Full field model describing phase front propagation, transformation strains, chemical partitioning and diffusion in solid-solid phase transformations

Aarne Pohjonen

October 19, 2022

1 Abstract

A novel mathematical formulation is presented for describing growth of phase in solid-to-solid phase transformations and it is applied for describing austenite to ferrite transformation. The formulation includes the effects of transformation eigenstrains, the local strains, as well as partitioning and diffusion. In the current approach the phase front is modelled as diffuse field, and its propagation is shown to be described by the advection equation, which reduces to the level-set equation when the transformation proceeds only to the interface normal direction. The propagation is considered as thermally activated process in the same way as in chemical reaction kinetics. In addition, connection to the Allen-Cahn equation is made. Numerical tests are conducted to check the mathematical model validity and to compare the current approach to sharp interface partitioning and diffusion model. The model operation is tested in isotropic two-dimensional plane strain condition for austenite to ferrite transformation, where the transformation produces isotropic expansion, and also for austenite to bainite transformation, where the transformation causes invariant plane strain condition. Growth into surrounding isotropic austenite, as well as growth of the phase which has nucleated on a grain boundary are tested for both ferrite and bainite formation.

Keywords: partial differential equations, mechanics of deformable solids, phase transformations, full field model, eigenstrains, diffusion

2 Introduction

The connection between the materials manufacturing processes and the physical mechanisms affecting the formation of the material microstructure is needed for accurately desribing the actual reality that is the fundamental cause for

the properties of the processed material. The capability of simulating the microstructure evolution provides important insight to the phenomena occurring in the industrial processes [1, 2]. Splitting the general observations in to separable phenomena, and providing quantitative description for each phenomena is the basis of the method of natural sciences, which has enabled the vast progress in modern science and technology. In addition to explaining separately the phenomena, also the interaction of the different basic phenomena produces new effects, that must be taken in to account in the full description of a process. Quantitative description of such dynamical effects requires advanced computational methods.

In our previous efforts of describing the mean field evolution of steel microstructure during processing [3], it was found that it is necessary to consider the detailed full field description of the microstructure evolution in order to include certain effects, such as stabilization of austenite due to increase of local carbon concentration and local stress caused by bainite formtion. Understanding of such phenomena is of paramount importance, since austenite stability decisively affects the mechanical properties of the steel [3]. In order to enable modelling of the phenomena, an effort to construct a fundamentally physics based full field model for solid-to-solid phase transformations was undertaken.

Solid-to-solid phase transformations have been modelled with several different methodologies capable of providing full field description of the phenomena. Such methods include e.g. the phase field [4, 5, 6, 7], level-set [8, 9, 10, 11] and cellular automata [12, 13, 14, 15] methods.

The phase field method applies the Allen-Cahn equaton [16] to describe the time evolution of the order parameter which characterizes the different phases and the Cahn-Hilliard equation [17, 18, 19] to describe the transport of mass within the phases and across the phase interfaces, which are diffuse in the phase field methodology. The Allen-Cahn equation [16] is similar to the time dependent Ginzburg-Landau equation, which was originally used for describing transition to superconductivity. The similar equation has been used for describing liquid-solid phase transition [20], liquid-vapour transition [21, 22] and solid-solid transitions [23]. Review of the phase field method is provided in [24] and [25].

The level-set method is a general method that can be applied for describing the movement of an interface. A function representing singed distance from the interface is usually applied as the propagating field, and the movement of the interface is calculated with a level-set equation. The phase propagation speed is used as an input of the model, hence the physics affecting the interface propagation can be implemented in the model, when the propagation speed can be calculated based on them [26, 27].

The cellular automata methods rely on constructing rules for the interface propagation, which can then be used for predicting the evolution of the system. The main difficulty in implementing real physical mechanisms in to cellular automata model is in implementing the rules that would represent the physical phenomena.

In the current study the focus is on providing physics based descripition

of the morphological evolution of ferritic region, which grows in to austenite, when steel has been cooled to sufficiently low temperature. The equation describing the phase interface movement is the advection equation which simplifies to the level-set equation, when the phase interface propagation occurs only in the interface normal direction. The interface propagation speed is determined based on the concept of thermal activation [28], which is also the basis of kinetic rate theory of chemical reactions [29]. The carbon partitioning and diffusion in austenite and ferritic regions is calculated by an unified equation, which has been earlier described e.g. in [5] and [30]. The eigenstrains of ferritic phase are introduced, and the resulting elastic strains are included in the model in the similar way as in [7, 6], but also different elastic constants for ferrite and austenite are considered in the current study. Equation describing the effect of the elastic strains to the activation energy barrier is derived. Numerical experiments were made to test the validity of the mathematical model and to demonstrate the coupled modelling of the phase front propagation, elasticity, carbon partitioning and diffusion in simplified two-dimensional settings. The results of numerical tests are presented for a case where austenite transforms to ferrite causing isotropic expansion, and also for a case where austenite transforms to bainitic ferrite, where the transformation causes another kind of strain state, the invariant plane strain.

3 Theory

3.1 Phase front propagation

In the current approach, a continuous differentiable field is applied to describe the region that has been transformed from initial phase to another phase. The model is applied to describe austenite to ferrite transformation in steel that has been cooled below equilibrium temperature. In reality, the transformation proceeds by nucleation of new ferritic regions in the austenite and the growth of the nucleated regions. The current study focuses in mathematical modelling of the growth the ferritic regions. In order to calculate the growth, an equation that describes the propagation of the phase front is required.

The phase field ϕ describes the transformed and untransformed regions. It is defined $\phi = 1$ for those regions that have been fully transformed to ferritic phase (α) and $\phi = 0$ for completely untransformed (austenitic, γ) regions. In the interface, between the transformed phase and the untransformed phase, the function ϕ changes continuously between 0 and 1. In the current study, a cosine function was applied to describe the transition from 1 to 0 as the distance from the nearest fully ferritic gridpoint increases, i.e. $\phi(r) = \frac{1}{2}(1 + \cos(r\pi/\Delta L))$, where $r \leq \Delta L$ is the shortest distance from the fully ferritic region and ΔL is the lenght of the transition region between ferrite and austenite. This condition was applied only in the initial definition of the field and the subsequent time evolution was described by solving Eq. (2).

Assume that a position of a material point at time t is $\vec{r} = (x(t), y(t), z(t))$.

If a field $\phi(\vec{r},t)$ is locally propagating inside of the material with velocity $\vec{v} = (v_x, v_y, v_z)$, the local evolution during timestep, $t \in [t_0, t_0 + \Delta t]$, is described as $\phi(\vec{r},t) = \phi(\vec{r} - \vec{v}t, t_0)$ and it's local time derivative can be calculated from Eq.(1).

$$\frac{\partial}{\partial t}\phi(\vec{r},t) = \frac{\partial \phi}{\partial x}\frac{\partial x}{\partial t} + \frac{\partial \phi}{\partial y}\frac{\partial y}{\partial t} + \frac{\partial \phi}{\partial z}\frac{\partial z}{\partial t} = -\nabla\phi \cdot \vec{v} \tag{1}$$

Eq. (1) is the *advection equation* and it is general in the sense that it describes the propagation of the field in any direction. In the current study, it is assumed that the phase boundary can only move forward or backward, i.e. to the direction of the iso-contour normal. The local normal of the isocontour of ϕ, directed in the negative direction of the gradient, is $\hat{n} = -\frac{\nabla\phi}{|\nabla\phi|}$. The local speed of the isocontour is defined as $s(\vec{r},t)$, and it depends on the local material conditions: the local stress/strain state and the local chemical concentration. Then $\vec{v} = s\hat{n}$ and Eq. (2) holds

$$\frac{\partial}{\partial t}\phi(\vec{r},t) = -\nabla\phi \cdot s\hat{n} = s|\nabla\phi| \tag{2}$$

The negative sign convention $\hat{n} = -\frac{\nabla\phi}{|\nabla\phi|}$ was adopted, since s describes the growth rate of the ferritic phase in to the austenite, which occurs to the direction of negative gradient of ϕ. It is noted that the advection equation is also used in the level-set formulation. Local curvature of the field, κ can be calculated as the divergence of $\hat{n}$, $\kappa = -\nabla \cdot \hat{n}$. [5]

3.2 Elasticity and transformation strains

The strain and stress fields were calculated by applying the theory of elasticity. The stress free transformation strains (eigenstrains) were introduced to the equations in a similar way as in [6], but in the current approach the mathematical description is augmented to handle also different elastic constants for austenite and ferrite.

For each material point in the initial coordinate system $\vec{w} = (w_1, w_2, w_3)$, the displacement field is defined as $\vec{u} = \vec{r}(t) - \vec{w}$, where $\vec{r}(t)$ is the material position at time t. The total strain field is calculated as $\epsilon_{kl}^{\mathrm{tot}} = (1-\phi)\epsilon_{kl}^{\gamma} + \phi\epsilon_{kl}^{\alpha}$, where ϕ is the local fraction of transformed phase, the austenite strain (or, in general, the strain of the untransformed phase) is $\epsilon_{kl}^{\gamma} = \frac{1}{2}\left(\frac{\partial u_k}{\partial w_l} + \frac{\partial u_l}{\partial w_k}\right)$, the ferrite strain is $\epsilon_{kl}^{\alpha} = \epsilon_{kl}^{\gamma} - \epsilon_{kl}^{00}$, and ϵ_{kl}^{00} is the stress free transformation strain (i.e. the eigenstrain of the transforming phase). The total strain simplifies to $\epsilon_{kl}^{\mathrm{tot}} = \epsilon_{kl}^{\gamma} - \phi\epsilon_{kl}^{00} = \frac{1}{2}\left(\frac{\partial u_k}{\partial w_l} + \frac{\partial u_l}{\partial w_k}\right) - \phi\epsilon_{kl}^{00}$, which is consistent with the expression given in [7]. The stress is defined for both austenite and ferrite phases as $\sigma_{ij}^{\gamma} = c_{ijkl}^{\gamma}\epsilon_{kl}^{\gamma}$ and $\sigma_{ij}^{\alpha} = c_{ijkl}^{\alpha}\epsilon_{kl}^{\alpha}$, where Einstein summation convention is applied. The total stress is $\sigma_{ij}^{\mathrm{tot}} = (1-\phi)\sigma_{ij}^{\gamma} + \phi\sigma_{ij}^{\alpha}$.

The change in elastic energy density is calculated as the mechanical work

done by the changing strains as described by Eq. (3)

$$\Delta E_{\text{mech}} = \int_{\epsilon_{ij}^{\text{tot}}}^{\epsilon_{ij}^{\text{tot}}+\Delta\epsilon_{ij}^{\text{tot}}} \sigma_{ij}^{\text{tot}} d\epsilon_{ij}'^{\text{tot}} \tag{3}$$

where $\Delta\epsilon_{ij}^{\text{tot}}$ is the change in the elastic strain and notation $d\epsilon_{ij}'^{\text{tot}}$ is used for the integration variable with respect to $\epsilon_{ij}^{\text{tot}}$, and Einstein summation is applied. If only the local phase fraction changes, $d\epsilon_{ij}^{\text{tot}}/d\phi = -\epsilon_{ij}^{00}$, thus the change in the elastic energy density due to the transformation is described by Eq. (4). This expression describes how much the energy changes as ϕ changes from its current value to $\phi + \Delta\phi$.

$$\begin{aligned}
\Delta E_{\text{mech}}^{\text{tr}} &= -\int_{\phi}^{\phi+\Delta\phi} \sigma_{ij}^{\text{tot}} \epsilon_{ij}^{00} d\phi' \\
&= -\int_{\phi}^{\phi+\Delta\phi} (1-\phi') c_{ijkl}^{\gamma} \epsilon_{kl}^{\gamma} \epsilon_{ij}^{00} + \phi' c_{ijkl}^{\alpha} \epsilon_{kl}^{\alpha} \epsilon_{ij}^{00} d\phi' \\
&= -\left[-\frac{(1-\phi')^2}{2} c_{ijkl}^{\gamma} \epsilon_{kl}^{\gamma} \epsilon_{ij}^{00} + \frac{\phi'^2}{2} c_{ijkl}^{\alpha} \epsilon_{kl}^{\alpha} \epsilon_{ij}^{00} \right]_{\phi'=\phi}^{\phi'=\phi+\Delta\phi}
\end{aligned} \tag{4}$$

Equation (4) can be used for evaluating the change in the mechanical energy due to phase transformation. It includes the description for different elastic constants for the transforming phase (α) and the untransformed phase (γ). The work related to expansion due to the phase transformation, as well as due to the shear are both included in the description. When the transformation proceeds to completition, ϕ' changes from the current value, ϕ, to one. In this case $\Delta\phi = 1 - \phi$.

The force $\vec{F}$ and the resulting acceleration of the material point is then calculated applying the Newton's second law, Eq. (5). [31, 4]

$$\vec{F} = \rho \frac{\partial^2 u_i(\vec{r}, t)}{\partial t^2} = \sum_j \frac{\partial \sigma_{ij}^{\text{tot}}(\vec{r}, t)}{\partial r_j} \tag{5}$$

In the static case the accelerations vanish and Eq. (6) holds.

$$\sum_j \frac{\partial \sigma_{ij}^{\text{tot}}(\vec{r}, t)}{\partial r_j} = 0 \tag{6}$$

3.3 Carbon partitioning and diffusion

The calculation of carbon partitioning from the ferritic phase to the austenitic phase as well as the concurrent diffusion in both phases is based on the approach described in [5, 30], which allows for using a single diffusion equation to describe the phenomena in both the austenitic and the ferritic phase. The total diffusion flux $\vec{f_C}$ at given location is given as weighted sum of the fluxes from

the austenitic phase and the ferritic phase as $\vec{f_C} = (1-\phi)D_\gamma^C \nabla C_\gamma + \phi D_\alpha^C \nabla C_\alpha$, where ϕ describes the local fraction of austenite transformed to ferrite. Since the total carbon concentration is conserved when only partitioning and diffusion is considered, the time dependence of the concentration is $\partial_t C = \nabla \cdot \vec{f_C}$, hence the time evolution equation for the concentration is described by Eq. (7).

$$\frac{\partial C}{\partial t} = \nabla \cdot [(1-\phi)D_\gamma^C \nabla C_\gamma + \phi D_\alpha^C \nabla C_\alpha] \tag{7}$$

Since the total amount of carbon is conserved, Eq. (8) holds.

$$C = (1-\phi)C_\gamma + \phi C_\alpha \tag{8}$$

Since the carbon concentration in austenite is non-zero, the fraction $k = C_\alpha / C_\gamma$ can be defined everywhere. It is assumed that at the interface the austenite and ferritic phases reach the equilibrium carbon concentration so that $k = C_\alpha^{\text{eq}}/C_\gamma^{\text{eq}} = C_\alpha^{\text{eq}}/(C - C_\alpha^{\text{eq}})$. Applying this definition of k and Eq. (8) yields $C_\alpha = kHC$ and $C_\gamma = HC$ where $H = 1/(1-\phi+\phi k)$. Substituting these quantities to Eq. (7) then yields the single equation that can be used to describe the carbon partitioning and diffusion, Eq. (9).

$$\frac{\partial C}{\partial t} = \nabla \cdot [(1-\phi)D_\gamma^C \nabla (HC) + \phi D_\alpha^C \nabla (kHC)] \tag{9}$$

The diffusion coefficients $D_\gamma^C = 2 \times 10^{-5} \times \exp(-140\text{kJ}/RT)$ and $D_\alpha^C = 2 \times 10^{-6} \exp(-10115/T) \times \exp(0.5898[1 + (2/\pi)\arctan(1.4985 - 15309/T)])$ [32], where R is the ideal gas constant (kJ is kilojoules), were used for the austenite and ferritic phases.

3.4 Propagation speed of the phase boundary

3.4.1 Thermally activated interface movement

In the current study it is assumed that the movement of the interface is thermally activated. This means that the growth rate is dictated by an energy barrier that needs to be overcome by thermal movement of the atoms at the interface. The energy barrier is defined by the local chemical composition, the difference of the local strain from the stress-free transformation strain, and the local interface energy between the phases. It is assumed that an austenitic atomic structure transforms to ferritic structure when the thermal vibration of the atoms overcomes the energy barrier for the transformation to occur at the interface. The frequency of the vibrations is the attempt frequency for the process ω. If the vibration is sufficiently energetic, it is succesful in transforming the local atomic unit cell from austenitic (γ) to ferritic (α) structure, which causes the interface to propagate a distance δ, which is the interatomic distance in austenite. In addition the transformation creates strains, which are taken in to account in the model as described in section 3.2. If the activation barrier for atoms to move from austenitic structure to the ferritic structure is $\Delta g^{\gamma\alpha}$, the

frequency of the process to occur is $\omega \exp(-\Delta g^{\gamma\alpha}/RT)$. If the corresponding activation barrier for the reverse process of moving atom from ferrite to austenite is $\Delta g^{\alpha\gamma} = \Delta g^{\gamma\alpha} + \Delta g^*$, where Δg^* is the difference between the forward and reverse processes, then the propagation speed is described by Eq. (10) [28].

$$\begin{aligned} s &= \delta\omega \left[\exp\left(-\frac{\Delta g^{\gamma\alpha}}{RT}\right) - \exp\left(-\frac{\Delta g^{\alpha\gamma}}{RT}\right) \right] \\ &= \delta\omega \exp\left(-\frac{\Delta g^{\gamma\alpha}}{RT}\right) \left[1 - \exp\left(-\frac{\Delta g^*}{RT}\right) \right] \end{aligned} \tag{10}$$

At the equilibrium transformation temperature, when equilibrium has been reached $\Delta g^* = 0$ and therefore $s = 0$. For small undercooling Δg^* is very small, $\Delta g^* << RT$. In this case $1 - \exp(-\Delta g^*/RT) \approx \Delta g^*/RT$, and then $s \approx (\Delta g^*/RT)\delta\omega \exp(-\Delta g^{\gamma\alpha}/RT)$. On the other hand, if the undercooling is sufficiently high so that $\Delta g^* >> RT$, then $1 - \exp(-\Delta g^*/RT) \approx 1$ meaning that practically no reverse transformation would occur. In this case $s \approx \delta\omega \exp(-\Delta g^{\gamma\alpha}/RT)$. The energy barriers are schematically illustrated in Fig. 1.

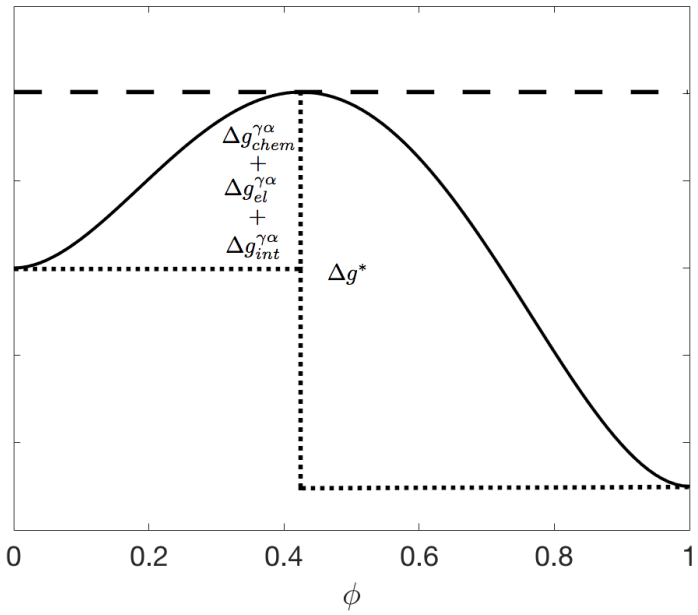

Figure 1: Schematic illustration of the energy change of the phase transition as function of ϕ and the associated energy barriers.

In order to relate the experimentally observable transformation speed to the theoretical description of the energy barriers, it is useful to consider an

effective or apparent activation energy, where the contributions from both of the quantities $\Delta g^{\gamma\alpha}$ and $\Delta g^{\alpha\gamma}$ are lumped together. For this purpose, and in the case that the transformation proceeds from austenite to ferrite, the Eq. (10) can be written as Eq. (11).

$$s = \delta\omega \exp\left(-\Delta G^{\gamma\alpha}/RT\right) \tag{11}$$

where $\Delta G^{\gamma\alpha} = \Delta g^{\gamma\alpha} + RT\ln\left[1 - \exp\left(-\frac{\Delta g^*}{RT}\right)\right]$ is the lumped overall effective energy barrier that needs to be overcome by the thermal movement of the interface atoms for the phase to propagate. The activation energy barrier can be separated in the components depending on the local elastic and interface contributions $\Delta g^{\gamma\alpha} = \Delta g^{\gamma\alpha}_{chem} + \Delta g^{\gamma\alpha}_{el} + \Delta g^{\gamma\alpha}_{int}$ and the thermodynamic driving force for the transformation $\Delta G^* = -RT\ln\left[1 - \exp\left(-\frac{\Delta g^*}{RT}\right)\right]$ so that the effective energy barrier is $\Delta G^{\gamma\alpha} = \Delta g^{\gamma\alpha}_{chem} + \Delta g^{\gamma\alpha}_{el} + \Delta g^{\gamma\alpha}_{int} - \Delta G^*$.

The elastic energy contribution to the energy barrier can be calculated from the change of mechanical energy that would result if material at the local position transforms as described by Eq. (12).

$$\Delta g^{\gamma\alpha}_{el} = \lambda \Delta E^{\mathrm{tr}}_{\mathrm{mech}} \tag{12}$$

where $\Delta E^{\mathrm{tr}}_{\mathrm{mech}}$ is the mechanical energy change due to transformation, evaluated from Eq. (4), where $\Delta\phi = 1 - \phi$. The parameter λ has the physical meaning, that it is the critical fraction of the total elastic energy density, which is required for changing the local strains ϵ_{kl} towards the stress-free transformation strain, ϵ^{00}_{kl}, so that the peak of the energy barrier $\Delta G^{\gamma\alpha}$ is reached. In a simple model, it can be used as a fitting parameter, but the value could in principle be obtained using atomistic simulations with the nudged elastic band method [33].

If the local strain is of the same sign as the stress-free transformation strain, the thermal fluctuation of the atoms required for the phase front to propagate is reduced, since less elastic energy is required for the transformation to complete. If they are of opposite sign, the barrier is increased. Since $\Delta g^{\gamma\alpha}_{chem}$ and ΔG^* can depend on the undercooling below the equilibrium temperature, the activation energy barrier is temperature dependent and since the local carbon concentration affects the chemical energy, the carbon partitioning and diffusion affects the transformation speed through this term. The removal of defects, such as the austenite grain boundary due to the movement of the austenite-ferrite interface can lower the energy barrier. The growth of ferrite along the austenite grain boundary is a result of this effect. The interface energy $\Delta g^{\gamma\alpha}_{int}$ depends on the crystal orientations of the neighbouring interfaces and the interface curvature κ. In an isotropic model, the crystal orientations do not have effect on the interface energy.

3.4.2 Connection between thermally activated phase propagation and Allen-Cahn equation

Similar related method for numerically simulating the full field evolution of phase transformations is the phase field method, based on the solution of the

Allen-Cahn equation, Eq. (13)

$$\frac{\partial \phi}{\partial t} = -\alpha \frac{\partial F}{\partial \phi} + M\nabla \cdot \nabla \phi \tag{13}$$

where the phase ϕ is described by the so-called order parameter. The connection between the Allen-Cahn equation and the equation for the phase propagation described in section 3.1 can be drawn by realizing that both methods yield an estimate for the time derivative of the field, which can be equated. This yields connection between the phase interface propagation speed s, described by Eq. (2), and the parameters of the Allen-Cahn equation, as described by Eq. (14).

$$s = \frac{1}{|\nabla \phi|}\frac{\partial \phi}{\partial t} = \frac{1}{|\nabla \phi|}\left[-\alpha \frac{\partial F}{\partial \phi} + M\nabla \cdot \nabla \phi\right] \tag{14}$$

The Eq. (14) could be used in conjunction with the Eq. (2) to calculate the phase front propagation in the same way as Eq. (11). However, in the current study, the Eq. (11) is applied in the numerical experiments (section 5) for calculating the speed of phase front propagation.

In the Allen-Cahn formalism, the free energy density F is usually represented as a 4th or 6th order polynomial function of ϕ. The energy barriers described by Eq. (10) are the differences between the local minimas and the maxima of this function, as schematically illustrated in Fig. 1. This connects the both approaches at the theoretical level. Suppose that $F(\phi) = F_{chem}(\phi) + F_{el}(\phi)$. To describe the chemical part, $F_{chem}(\phi)$ phenomenological polynomials are usually applied, which can be also obtained from the CALPHAD method [24]. The elastic part F_{el} is described by Eq. (4) by setting the lower bound of the integral to zero and the upper bound to ϕ. Then the critical value ϕ_{max} where the function obtains it's local maxima, as well as the local minimas $\phi_{min1} = 0$ and $\phi_{min2} = 1$ can in principle be found by solving $dF(\phi)/d\phi = 0$. From the obtained values, the energy barriers of Eq. (10) could then be calculated. The phenomenological parameter in Eq. (12) is then $\lambda = \int_{\phi}^{\phi_{max}} \Delta E^{tr}_{mech} / \int_{\phi}^{1} \Delta E^{tr}_{mech}$. The black solid line in Fig. 1 schematically illustrates the function $F(\phi)$. The propagation speed calculation using the thermally activated description, where the energy barrier heights were applied, is another way of looking the energetic principles of the same problem as the Allen-Cahn formalism. Both approaches involve phenomenological parameters, which can be calibrated, based on experiments or by using thermodynamical database.

4 Numerical solution procedures

There are several ways to obtain the solution to the partial differential equations, such as finite element analysis, finite volume method or finite difference method, where each approach has it's own strengths. The aim of this section is to describe the practical issues related to the numerical solutions of the derived Eqs (2), (11), (6) and (9), which determine the phase front propagation, elastic strains and

partitioning and diffusion of carbon in a coupled way. Because elastic strains, which are caused by the phase transformation, move the material points, and since the values are evaluated at the material points, the numerical grid becomes deformed due to the transformation. In the current study, the numerical solution to the partial differential equations was obtained by the method described in [34], which is capable of providing the solution to the equations in deformed grids and is reasonably simple and straightforward to implement.

The numerical solution of Eq. (2) requires a special attention, as discussed in [35]. Despite it's seeming simplicity, the straightforward solution of calculating the first order spatial derivatives and applying the Euler forward approximation in time yields solution which is unstable in a standard finite difference scheme [35]. In the current approach described in [34], this approach was found to result in broadening of the phase front. A remedy was found by setting the time derivative to zero at the gridpoints that were further away from the fully transformed region than the interface width. In addition an average time derivative was calculated from the neighbouring gridpoint values and applying it in the Euler forward time step, i.e. the averaged time derivative for gridpoint index (I, J, K) is calculated by averaging the gridpoint values where the gridpoint indices $i \in [I-1, I, I+1]$, $j \in [J-1, J, J+1]$ and $k \in [K-1, K, K+1]$. This procedure is described in detail in [36].

The method [34] provides a way to calculate the first and second order spatial derivatives of the field. As described in [34], a correction procedure was introduced to enhance the convergence of the solution for the second order spatial derivatives. This correction procedure requires to identify the gridpoints that contain the local maximas/minimas of the field and the local first order derivatives near the local maximas/minimas. For this reason it is needed to write out the evolution equations (5) and (9) to explicitly include the first and second order derivatives of the fields so that the correction procedure can be applied.

The local force given by Eq. (5) can be re-written as Eq. (15).

$$\vec{F} = \sum_j \frac{\partial \sigma_{ij}(\vec{r}, t)}{\partial r_j} = \frac{\partial c_{ijkl}}{\partial r_j} \epsilon_{kl} + c_{ijkl} \frac{\partial \epsilon_{kl}}{\partial r_j} \tag{15}$$

where Einstein summation convention is applied and $\frac{\partial \epsilon_{kl}}{\partial r_j} = \frac{1}{2}\left(\frac{\partial}{\partial r_j}\frac{\partial u_k}{\partial w_l} + \frac{\partial}{\partial r_j}\frac{\partial u_l}{\partial w_k}\right) + \frac{\partial \phi}{\partial r_j}\epsilon^{00}_{kl}$. This expression was used in the numerical calculations so that the correction procedure described in [34] can be be applied for the second order derivatives $\frac{\partial}{\partial r_j}\frac{\partial u_k}{\partial w_l}$ and $\frac{\partial}{\partial r_j}\frac{\partial u_l}{\partial w_k}$ when the numerical gridpoints containing the local maximas/minimas of u_k and u_l, as well as the values of $\frac{\partial u_k}{\partial w_l}$ and $\frac{\partial u_l}{\partial w_k}$ at the gridpoints neighbouring the maximas/minimas are first determined from the first order differentiation of u_k and u_l, as described in [34].

The diffusion coeffients D^c_γ and D^c_α are assumed as constants with respect to position. The diffusion Eq. (9) can be re-written as Eq. (16), which then

contains first and second order spatial derivatives of functions ϕ, HC and kHC

$$\frac{\partial C}{\partial t} = \nabla\phi \cdot \left[-D_\gamma^c \nabla(HC) + D_\alpha^c \nabla(kHC)\right] + (1-\phi) D_\gamma^c \nabla^2(HC) + \phi D_\alpha \nabla^2(kHC) \tag{16}$$

Once the derivatives are calculated with the method presented in [34], the time evolution of the system was calculated using Euler forward difference approximation, i.e. $C(\vec{r}, t_0 + \Delta t) = C(\vec{r}, t_0) + \frac{\partial C}{\partial t}|_{t_0} \Delta t$.

It was observed from the calculations of the energy barrier for the example cases, that it is the austenite side of the interface which determines the rate of phase propagation, since the energy barrier, which is affected by the mechanical energy and austenite carbon concentration was always higher on the austenite side of the interface. For this reason, it was chosen that the phase propagation speed was calculated at the grid points, that were located at next to (at both sides) the curve which passes through the middle of the austenite side of the interface, i.e. the contour plot $\phi = 0.25$, shown with the red dashed line in Fig. 2. The values that were calculated at these grid points were then dispatched to the neighbouring points within radius $R_{\text{avg}} = 5.25\Delta x = 8.14 \times 10^{-8}$ m, indicated by the interior of the red dotted line for an example point indicated with red dot in Fig. 2 b). The value $\Delta x = 1.55 \times 10^{-8}$ is the undeformed grid point spacing. Before dispatching the value to the gridpoints, the interface orientation of the gridpoints was evaluated and it was used in the calculation of the propagation speed of the interface segment: the local interface vector $\vec{n}_{loc}$ (at the red dot) was calculated. For each gridpoint within the dispatched region (the red dotted circle) the interface normal vector $\vec{n}_{disp}$ was also used. The propagation speed was dispatched for all the interface gridpoints where $\vec{n}_{loc} \cdot \vec{n}_{disp} \geq 0$. The weighted average of the dispatched values was then used for calculating the local speed for the gripoint, where the values $\vec{n}_{loc} \cdot \vec{n}_{disp}$ were used as the weights. This procedure allowed to maintain local average speed for the an interface segment. To diminish possible broadening of the interface, the interface speed was set to zero if the smallest distance from the region where $\phi \geq 0.9$ became larger than $D_{\max} = 5.25dx = 8.14 \times 10^{-8}$ m. The above mentioned values of dx, R_{avg} and $D_{\max}$ were used in the example cases in this article.

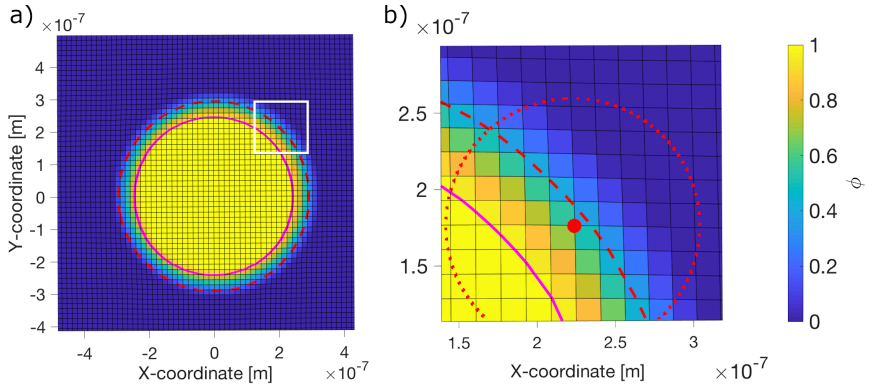

Figure 2: a) Overall phase field, b) zoom to the local interface segment region. The interface propagation speed was calculated at grid points located next to the iso-contour $\phi = 0.25$ (red dashed line). The value was dispatched to the neighbouring gridpoints (within red dotted line in b)). The phase propagation was set to zero if the interface distance from the iso-contour $\phi = 0.9$ (magenta solid line) was larger than $D_{\max}$.

5 Numerical experiments

To check that the model provides an useful tool for describing growth phenomenon in solid-solid phase transformations and the applied numerical method provides correct results, numerical experiments were conducted. The aim was to first test the different parts of the model separately. After this the full model is applied in describing few selected example problems, where the phase propagation, transformation stress/strain calculation as well as partitioning and diffusion are modelled in a coupled way. For simplicity, in the following example cases isotropic 2-dimensional model was considered. Plane strain conditions were applied for the elasticity calculations. The elastic constants of austenite and ferrite were assumed to be equal, i.e. the approximation $c^{\gamma}_{ijkl} \approx c_{ijkl} \approx c^{\alpha}_{ijkl}$ was used. The non-zero elastic constants for these conditions are described by the Eqs. (17,18,19).

$$c_{1111} = \frac{E}{1-2v} = c_{2222} \tag{17}$$

$$c_{1122} = \frac{Ev}{(1+v)(1-2v)} = c_{2211} \tag{18}$$

$$c_{1212} = \frac{E}{(1+v)} = c_{2121} \tag{19}$$

where the values $E = 200$ GPa and $v = \frac{1}{3}$ were used. The elastic energy barrier for phase front propagation is calculated from Eqs. (3) and (12). Since $c^{\gamma}_{ijkl} \approx c_{ijkl} \approx c^{\alpha}_{ijkl}$, the elastic energy barrier is $\Delta g_{el} = \lambda \Delta E^{\mathrm{tr}}_{\mathrm{mech}}$, where

$$\begin{aligned}\Delta E^{\mathrm{tr}}_{\mathrm{mech}} &= -\int_{\phi}^{1} c_{ijkl}(\epsilon^{\gamma}_{kl} - \phi'\epsilon^{00}_{kl})\epsilon^{00}_{ij}\, d\phi' \\ &= -\left[c_{ijkl}\epsilon^{\gamma}_{kl}\epsilon^{00}_{ij}\phi' - c_{ijkl}\epsilon^{00}_{kl}\epsilon^{00}_{ij}\frac{\phi'^2}{2}\right]_{\phi'=\phi}^{\phi'=1}\end{aligned} \tag{20}$$

and Einstein summation convention is applied. Componentwise expressions for the elastic energy densities can be written such that $\Delta E^{\mathrm{tr}}_{\mathrm{mech}} = \Delta E^{\mathrm{tr}}_{\mathrm{mech11}} + \Delta E^{\mathrm{tr}}_{\mathrm{mech22}} + \Delta E^{\mathrm{tr}}_{\mathrm{mech12}} + \Delta E^{\mathrm{tr}}_{\mathrm{mech21}}$, where

$$E^{\mathrm{tr}}_{\mathrm{mech11}} = \frac{1-\phi^2}{2}(c_{1111}\epsilon^{00}_{11}\epsilon^{00}_{11} + c_{1122}\epsilon^{00}_{22}\epsilon^{00}_{11}) - (1-\phi)(c_{1111}\epsilon^{\gamma}_{11}\epsilon^{00}_{11} + c_{1122}\epsilon^{\gamma}_{22}\epsilon^{00}_{11}) \tag{21}$$

$$E^{\mathrm{tr}}_{\mathrm{mech22}} = \frac{1-\phi^2}{2}(c_{2222}\epsilon^{00}_{22}\epsilon^{00}_{22} + c_{2211}\epsilon^{00}_{11}\epsilon^{00}_{22}) - (1-\phi)(c_{2222}\epsilon^{\gamma}_{22}\epsilon^{00}_{22} + c_{2211}\epsilon^{\gamma}_{11}\epsilon^{00}_{22}) \tag{22}$$

$$E^{\mathrm{tr}}_{\mathrm{mech12}} = \frac{1-\phi^2}{2}c_{1212}\epsilon^{00}_{12}\epsilon^{00}_{12} - (1-\phi)c_{1212}\epsilon^{\gamma}_{12}\epsilon^{00}_{12} \tag{23}$$

$$E^{\mathrm{tr}}_{\mathrm{mech21}} = \frac{1-\phi^2}{2}c_{2121}\epsilon^{00}_{21}\epsilon^{00}_{21} - (1-\phi)c_{2121}\epsilon^{\gamma}_{12}\epsilon^{00}_{21} \tag{24}$$

The value for the speed of sound was used for the pre-factor of the exponential function, $\delta\omega = 5900$ m/s. The composition dependent part of the energy barrier was assumed as $\Delta g^{\gamma\alpha}_{chem} = 190$ kJ/mol for ferrite and $\Delta g^{\gamma\alpha}_{chem} = 142$ kJ/mol for bainite. The value for $0 < \lambda \leq 1$ was varied for different cases. To introduce the effect of local carbon concentration to the activation energy barrier, the function $\Delta G^* = [-24.3\times10^3 + 0.43(C - C_0)]$ J/mol was used, where C is the local carbon concentration, and $C_0 = 19482$ is the initial austenite carbon concentration in mol/m^3. In this way, the increase in the local carbon concentration increases the local energy barrier for the phase transformation. However, the aim of the current study is only to show the operation of the developed mathematical model, and the applied parameter values were not calibrated. This can be the subject of future studies, where the model parameters can be deduced based on experimental data or thermodynamic software. For simplicity of interpreting the results, the following example cases were conducted using constant temperature. Clearly, the model allows also for calculations using changing temperature as will, which will affect the diffusion and growth rates through the Eqs. 9 and 10.

5.1 Numerical experiment 1: Growth of phase with predetermined interface velocity field

To check that the Eq. (2) and it's numerical solution provide suitable description for the phase interface propagation when the speed of the interface normal is pre-scribed, the following numerical experiment was conducted. First for each direction, propagation speed was pre-scribed as function of $\theta = atan2(y, x)$ [37].

In this way, the propagation speed is prescribed as any function of theta, and it can be determined by fitting for a given figure. To give an example, the heart symbol was chosen. The points picked to depict the shape are shown in Fig. 3 a).

In the simulation, the propagation speed was determined as function of the angle between the phase interface normal vector and the x-axis. During the simulation, the speed could be then calculated for each interface point, based on the orientation of the interface normal vector. Once the propagation speed was defined in this way, the growth from an initial small cylindrical field yielded the shape of the fitted function, as shown in the Fig. 3 b). The growth of the phase region at different steps are shown in c)-f).

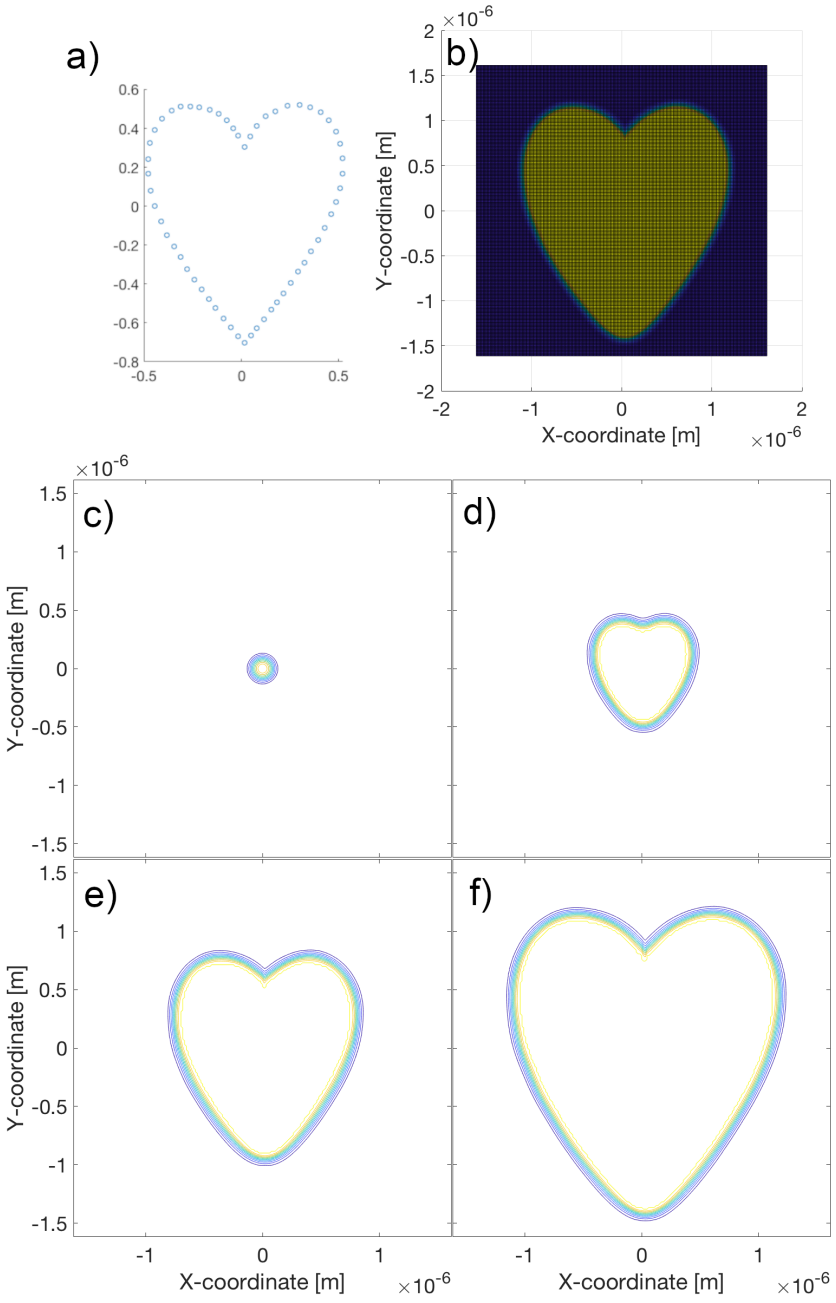

Figure 3: Growth of the phase field under pre-scribed interface propagation speeds. a) The points of the shape that was used for defining the interface propagation speeds at different direction from the origin. b) Resulting shape after growth. c)-d) the contour plots of the simulation for intermediate steps during the growth.

5.2 Numerical experiment 2: Elastic deformation of material surrounding growing expanded cylindrical region

To confirm that the Eq. (6) describing the elastostatic condition is correctly solved, the numerical solution was compared to the analytical solution available for a simple case, which is similar to the conditions prevailing in the growth of the phase region that introduces transformation strains inside the region. The chosen test case was the elastic deformation of the material surrounding an enlarged cylindrical region, which grows at constant rate. For the comparison, it is assumed that the growth rate of the cylindrical region is sufficiently slow, so that the material is in elastostatic equilibrium described by Eq. (6).

The simulation domain was a square region with 3.24 μm side length. The boundaries of the simulation region were fixed, i.e. the displacement field $\vec{u} = 0$ was set at boundaries for every time instant. The stress-free transformation strains (eigenstraines) in cartesian coordinates inside the transformed phase region were chosen as $\epsilon^{00}_{xx} = 0.1 = \epsilon^{00}_{yy}$ and zero otherwise. The local eigenstrain field was dependent of the fraction ϕ of transformed phase, calculated as $\phi\epsilon^{00}_{xx}$ and $\phi\epsilon^{00}_{yy}$.

The analytical elastostatic solution describing the plane axisymmetric deformation under plane-strain conditions [38] for the stress in the radial direction, σ_{rr} is described by Eq. (25)

$$\sigma_{rr} = \frac{E}{(1+v)(1-2v)}\left(C_1 - (1-2v)C_2\frac{1}{r^2}\right) \tag{25}$$

The determination of the stress field caused by the transformation strains (eigenstrains) is known as the Eshelby's inclusion problem. Analytic solutions exist for simple geometries and, in the context of current study, they are useful for comparing the numerical result to them. The elastostatic stress tensor component σ_{xx} inside of the cylindrical region with eigenstrains ϵ^{00}_{xx} and ϵ^{00}_{yy}, surrounded by elastic medium, is given by Eq. (26). [39]

$$\sigma_{xx} = -\frac{E}{2(1+v)}\left(\frac{3}{4(1-v)}\epsilon^{00}_{xx} + \frac{1}{4(1-v)}\epsilon^{00}_{yy}\right) \tag{26}$$

To check that the numerical method provided correct result, the numerical elastostatic solution was compared to the analytical solution given by Eq. (25) and (26). When plotted along a line, which passes through the center of the cylindrical region, and is directed along the x-direction, $\sigma_{xx} = \sigma_{rr}$. This allows for comparison of the numerical result against the analytical solution given by Eqs. (25) and (26). Continuity of the stress field and the stress near the simulation region boundaries were used to determine the constants C_1 and C_2 in Eq. (25). Strictly, the analytical solution describes the stress field in an infinite medium, but since the simulation domain was sufficiently large in comparison to the cylindrical region, the solutions can be compared. The comparison between the numerical and analytical solutions for cylindrical transformed region of 0.21 μm radius is shown in Fig. 4.

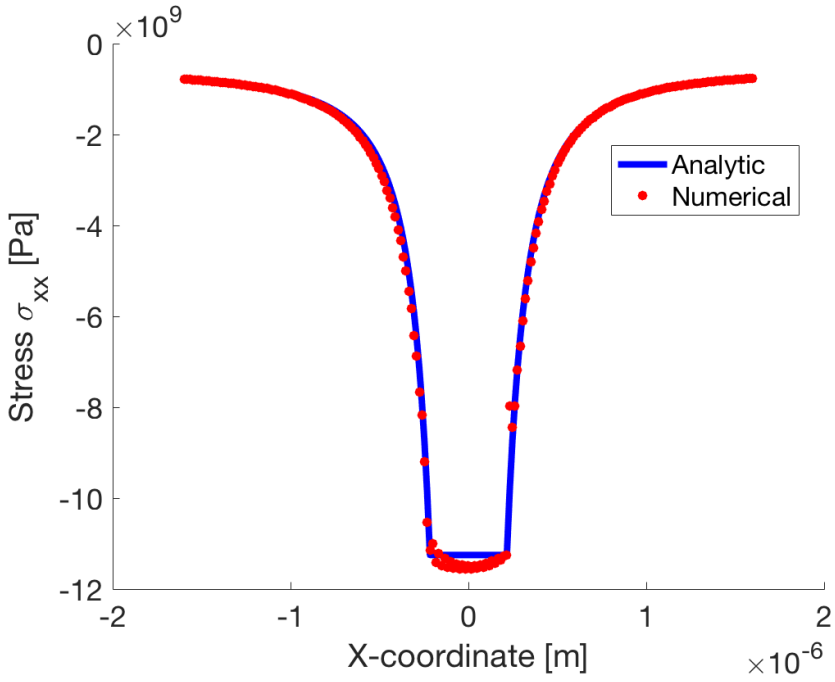

Figure 4: Comparison between the numerical elastostatic solution and the analytical solution for the stress σ_{xx} in a system containing enlarged cylindrical region, described by Eq. (25) and (26).

The elastostatic calculation was performed for each time step for the growing cylindrical region, which was initiated at the origin. The initial phase was a single gridpoint located at the origin. As described in section 3.1, the function $\phi(r) = \frac{1}{2}(1 + \cos(r\pi/\Delta L))$ was used to describe the transition from $\phi = 1$ (transformed) to $\phi = 0$ (untransformed) during the initialization of the phase field. The transformed phase region was assumed to propagate with constant speed in all directions, so that the phase region retained the shape of a cylinder with radius increasing at constant speed. Thus the model described radial growth of an enlarged cylindrical region within a rectangular domain where the boundaries were fixed, under plane strain conditions.

The stress field outside of the cylidrical region at different times during the growth was compared to the analytical solution, Eq. (25), as shown in Fig. 5 a). The contour circles in the inset figure show the size of the region at different simulation times. The value of the stress in a) was plotted along the dashed line shown in b). The values of the stress tensor components in the region close to the enlarged cylindrical region indicated with the green contour are shown in Fig. 5 b)-d).

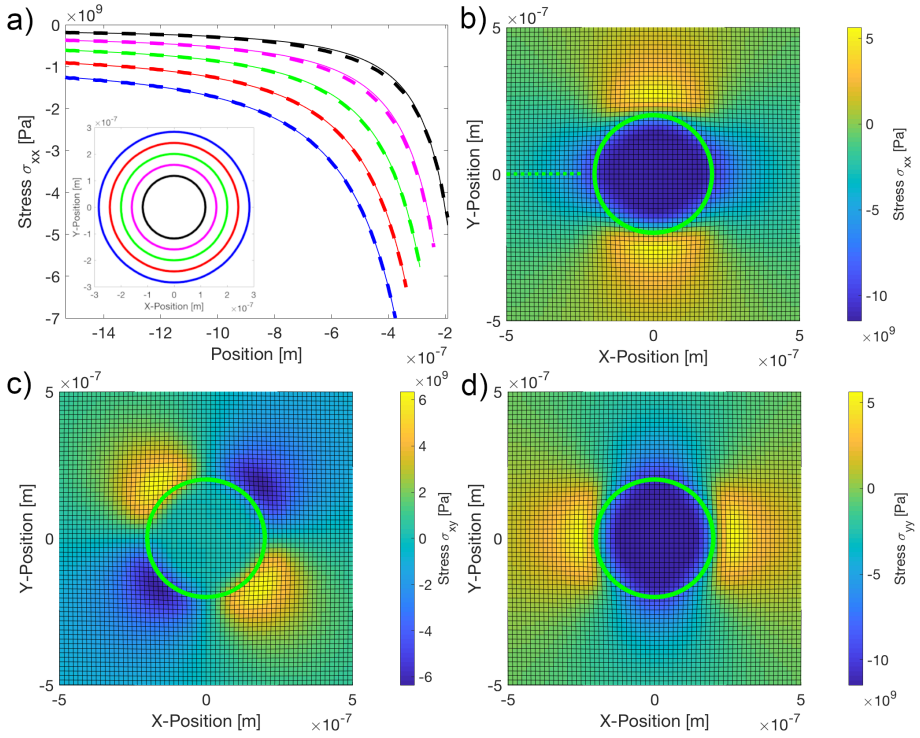

Figure 5: Stress fields calculated (dashed lines) in a domain containing cylindrical region with eigenstrains $\epsilon_{xx}^{00} = 0.1 = \epsilon_{yy}^{00}$ and a) comparison to the analytic solution (solid lines), σ_{xx} is plotted along a line directed in the x-direction and passing through origin for different sized regions shown in the inset. The plot line is shown in b) for the region depicted with green contour. The components of the stress tensor σ_{ij}^{tot} are shown in c)-d) for the same region.

5.3 Numerical experiment 3: Partitioning and diffusion of carbon from ferritic region to austenitic region over immobile boundary

The Eq. (9) enables the calculation of partitioning and diffusion of carbon in austenitic and ferritic regions. It is not immediately obvious how partitioning of chemical elements described by the Eq. (9) over the diffuse interface corresponds to a sharp interface. To see the correspondence of these cases, the diffuse model described by Eq. (9) was compared to the one dimensional sharp interface model for partitioning and diffusion of carbon that was applied in the previous publication [40]. For performing the comparison in a simplified setting, it was assumed that equilibrium carbon concentration in the ferrite is $C_{\alpha}^{\mathrm{eq}} = 0.02$ wt % carbon and then the equilibrium factor $k = C_{\alpha}^{\mathrm{eq}}/C_{\gamma}^{\mathrm{eq}} = 0.02/(1 - 0.02)$. It was observed that although qualitatively the concentration in the ferrite calculated

by the diffuse interface model was quite close to the result obtained by the sharp interface model for the short timescales (less than 1 s), the ferrite side of the interface stayed at higher concentration than the equilibrium concentration. For this reason, an adjustment parameter p was applied to calibrate the diffuse interface model, $k = pC_\alpha^{\mathrm{eq}}/C_\gamma^{\mathrm{eq}} = p0.02/(1-0.02)$ so that the correct equilibrium concentration was achieved in the ferrite region after all of the carbon had partitioned to austenite. When the diffuse interface length was $5dx$, where $dx = 1.5502 \times 10^{-8}$ m is the grid point spacing in undeformed state, it was found that the value $p = 0.5$ provided good correspondence between the two cases, and this calibrated value was applied in all consecutive simulations.

The carbon concentration in the ferrite region during the rapid partitioning as well as the concentration field after 4 seconds is shown and compared to the sharp interface result in Fig. 6. The carbon concentration field over the interface boundary is shown and compared to the sharp interface result in Fig. 7. It can be seen that the austenite carbon concentration is spread more uniformly in the diffuse interface model than in the sharp interface model. Consequently the carbon peak becomes flattened in the diffuse interface model. As time passes and the carbon is diffused further into the austenite, the results of the two models become similar. Thus in applying the diffuse interface model, the applied interface thickness affects the result, and it needs to be specified and taken in to account when comparing the results.

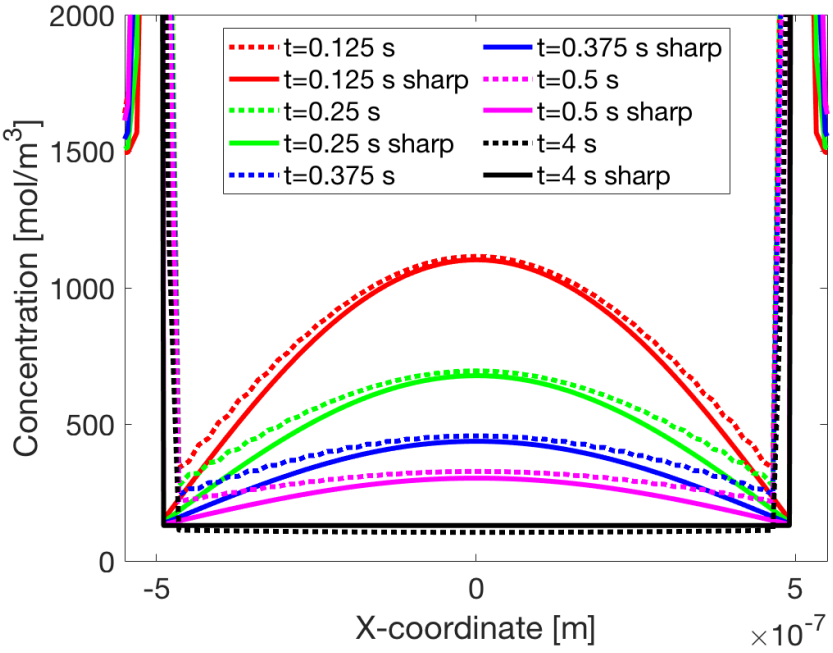

Figure 6: The carbon concentration field in the ferritic region calculated with the current diffuse interface model, Eq. (9), and compared to the previous sharp interface model, which was applied in [40].

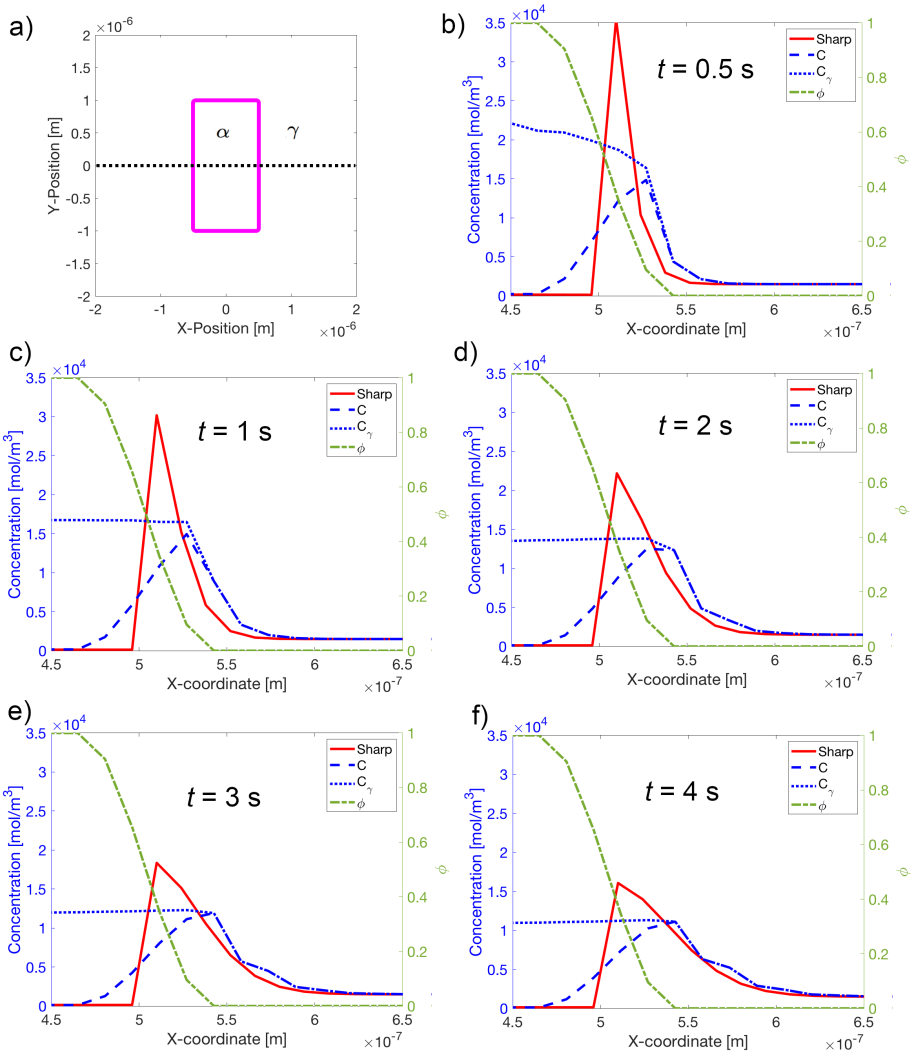

Figure 7: The carbon concentration field over the interface calculated with the current diffuse interface model, Eq. (9) and compared to the previously applied sharp interface model [40]. a) Simulation domain was divided in to a rectangular ferritic region (α) and the surrounding austenite (γ). The concentration field was analyzed along the black dashed line. b)-f) carbon concentration field at different simulation times. The plotted value of ϕ shows the gradual change between the austenite and ferrite regions in the diffuse interface model, where $\phi = 1$ for ferrite and $\phi = 0$ for austenite. $C_\gamma = HC$ shows the carbon concentration in austenite within the interface.

5.4 Numerical experiment 4: Isotropic growth of homogeneously nucleated ferrite

To test the model, a simulation of the growth of a homogeneously nucleated ferrite in a surrounding austenite was conducted. The two dimensional plane strane setting described earlier was applied. The growth rate was assumed to not depend on any crystal orientation and the value $\lambda = 0.9$ was used. The temperature was set to $T = 700$ °C. The ferrite formation was assumed to cause isotropic expansion with eigenstrains $\epsilon^{00}_{xx} = 0.05 = \epsilon^{00}_{yy}$. Although ferrite usually nucleates heterogeneously at crystal defects, such as grain boundaries, it is necessary to check that the model calculations yield the isotropic growth, which must occur if there is no orientation preference. Also, the resulting strain and carbon concentration fields provide a reference that can be used for comparison to the anisotropic growth case where the ferrite region nucleates and grows on the grain boundary, described in section 5.5.

In small scale, there can be slight deviation from the absolute circular shape, since the computational grid is discrete. However, the smoothly changing interface effectively yields circular curvature around the ferrite region. To make sure that the initial condition before the growth is simulated is as isotropic as possible, and not affected too much by any numerical errors due to discrete numerical grid, the initial ferrite region was chosen to contain the gridpoints contained within 1.32×10^{-7} m radius from the origin. To make sure that the carbon concentration was uniform before the growth started, the interface speed was set to zero for the first 0.0058 s, so that the carbon was able to partition uniformly from ferrite to austenite before the interface movement was started.

The initial ferrite region depicted in Fig. 8 a) and its growth in b), c) and d).

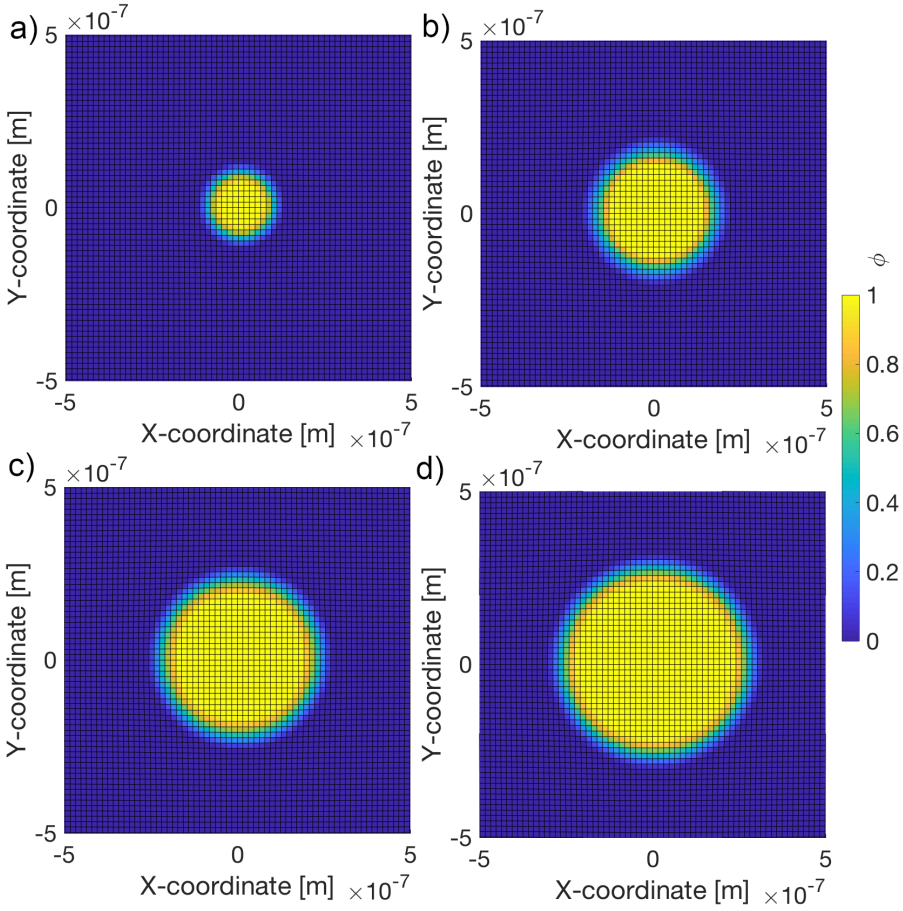

Figure 8: Isotropic growth of a ferrite region which was assumed to have been homogeneously nucleated in a surrounding austenite. The ferrite eigenstrains were $\epsilon^{00}_{xx} = 0.05 = \epsilon^{00}_{yy}$. The simulation snapshots at time instants a) 2.587×10^{-4} s, b) 0.0290 s, c) 0.0482 s d) 0.0646 s.

The mechanical energy for ferrite formation and the austenite strains ϵ^{γ}_{ij} in the regions where ferrite has not been fully formed (i.e. where $\phi < 1$) are depicted in Fig. 9 when $t = 0.0646$ s. The carbon concentration at the same time instant is shown in Fig. 10 a) and b). The concentration field was plotted in c) along the three lines shown in a). The plots almost fully overlap, only some small numerical difference can be seen right next to the interface. Also the phase field ϕ was plotted in d) along the same three lines to check that the growth rate had been isotropic in these directions. It can be seen that also in this case the plots overlap, confirming the isotropic growth.

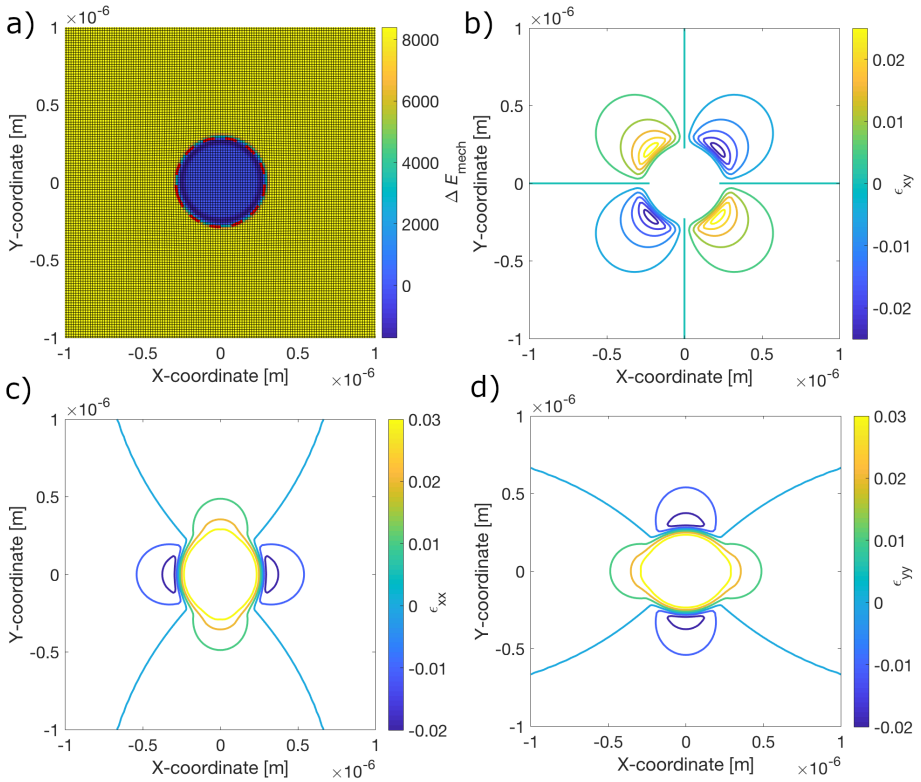

Figure 9: a) Change of mechanical energy due to transformation calculated with Eq. (20) for ferrite growth to surrounding austenite of the siulation snapshot depicted in Fig. 8 d). The red dashed line shows contour for $\phi = 0.25$. The austenite strains b) ϵ^{γ}_{xy} c) ϵ^{γ}_{xx}, d) ϵ^{γ}_{yy}. The non-zero ferrite eigenstrains were $\epsilon^{00}_{xx} = 0.05 = \epsilon^{00}_{yy}$.

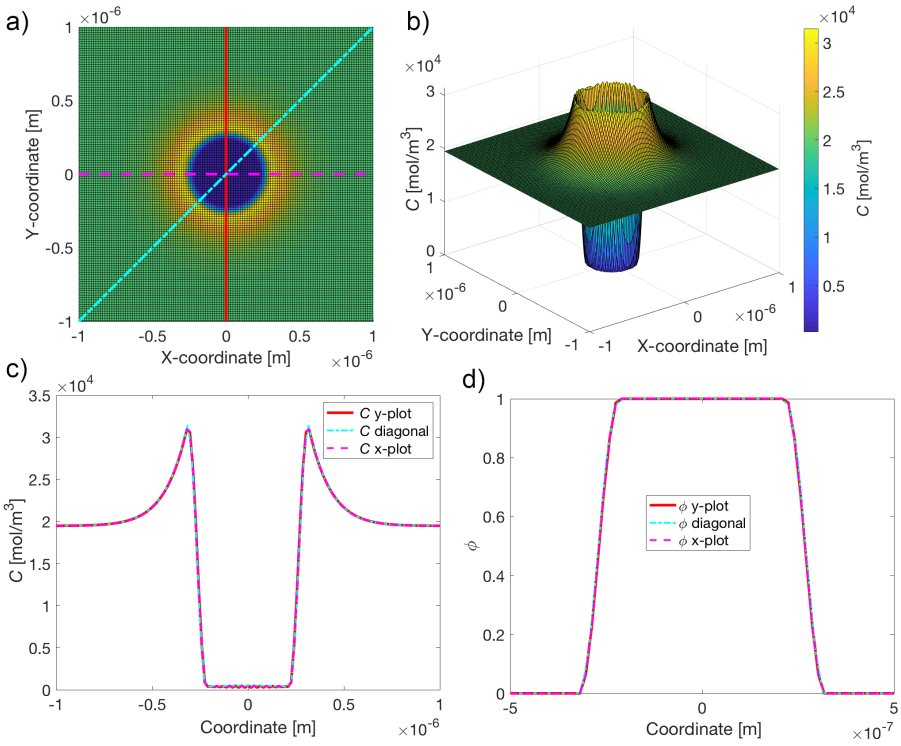

Figure 10: The carbon concentration of a ferrite region a), which was homogeneously nucleated and grew in to the surrounding austenite depicted in Fig. 8 d). The concentration was analyzed along three different lines, the plots are shown in c). The 3-D plot of the concentration is shown in b). The plot of ϕ along the same three lines is shown in Fig. d). In c) and d) the lines overlap, indicating isotropic growth, partitioning and diffusion.

5.5 Numerical experiment 5: Growth of allotriomorphic ferrite

Since grain boundaries involve atomic lattice mismatch, they are at a higher energy state compared to a perfect crystal. When a ferrite nucleates and grows on the grain boundary, the process can lower the local energy density. For this reason, it is energetically favorable for the ferrite to nucleate at the grain boundary and grow along it, in comparison to perfect crystal. In this case, the growth speed is decisively influenced by the grain boundary, and the resulting ferrite structure is called as an allotriomorphic ferrite [41]. In reality, also the crystal orientations of the neighbouring austenite grains affect the higher energy state caused by the lattice mismatch. The nucleating ferrite is likely to have energetically favourable orientation to neighbouring austenite grains, and in addition the growth speed in certain crystal directions could be higher, depending on

the neighbouring ferrite and austenite orientations over the interface direction. [42] However, in the current study, the aim is to test the mathematical model in a simplified setting, and the effect of the crystal orientations is completely neglected. For the testing purpose, it is assumed that the removal of the austenite grain boundary due to ferrite growth yields a change of -15 kJ/mol in the energy barrier for interface propagation for the gridpoints that are contained in the grain boundary. In the current study the value was picked so that the operation of the model could be tested, i.e. the order of magnitude is such that it yields reasonable effect in the results. In the future studies, the value could be more accurately calibrated based on experimental data and/or atomistic simulations, which enable the calculation of the interface energies. The application of the atomistic simulation methods also would allow for incorporating the effect of crystal orientation on the interface energies. The ferrite eigenstrains and the parameter λ were the same as for the previous case, section 5.4.

First, a simulation of the growth of a ferrite region nucleated on a flat grain face was conducted. The grain boundary was introduced in the simulations as depicted in Fig. 11 with the red dashed line. The ferrite nucleus was introduced at the origin, so that the grain boundary passes through it. The subsequent growth of the ferrite region is shown in Fig. 11 b)-d).

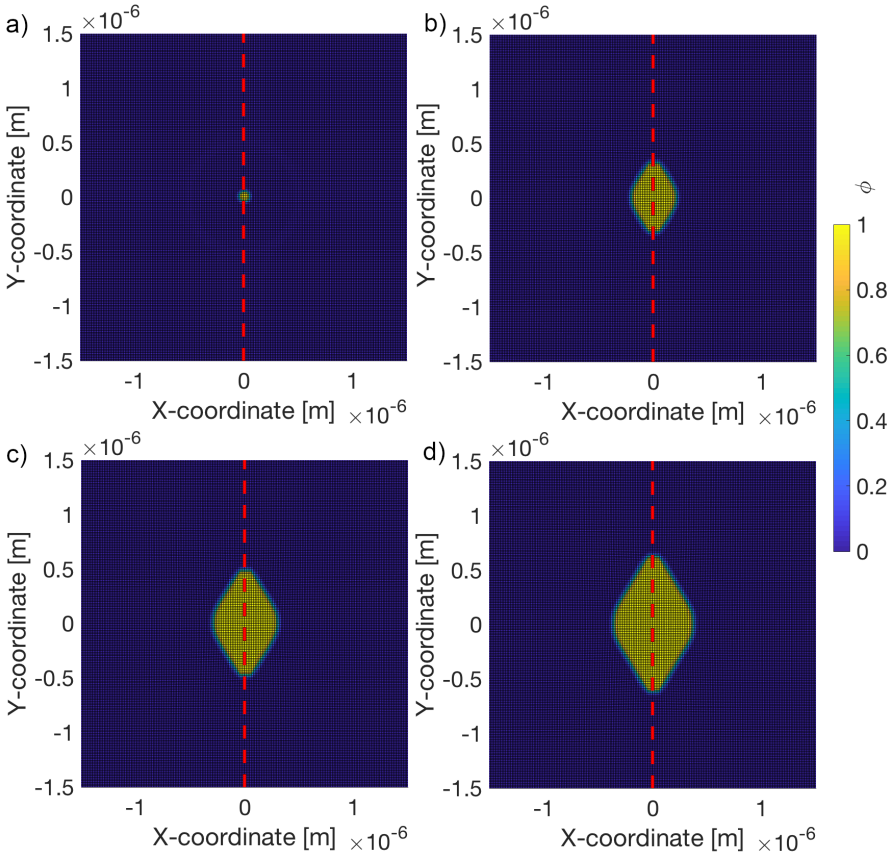

Figure 11: Growth of a ferrite region nucleated at a grain face. The grain boundary is depicted with a red dashed line. Simulation snapshots at time instants a) 0.0047 s, b) 0.0605 s, c) 0.09806 s d) 0.1340 s.

The mechanical energy for ferrite formation, and the austenite strains ϵ_{ij}^{γ} in the regions where ferrite has not been fully formed (i.e. where $\phi < 1$), are depicted in Fig. 12 for the time instant $t = 0.1340$ s. The carbon concentration at the same time instant is shown in Fig. 13 b) and c). The concentration was plotted along the three lines shown in c), the plots are shown in d).

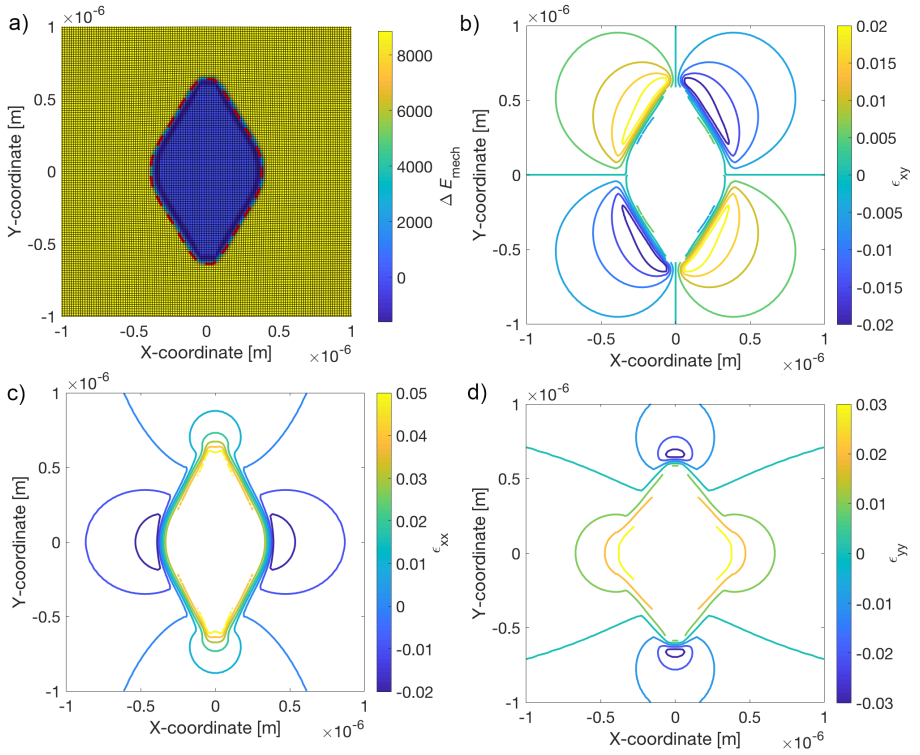

Figure 12: a) Change of mechanical required for the transformation calculated with Eq. (20) for ferrite nucleated at grain face depicted in Fig. 11 d). The red dashed line shows contour for $\phi = 0.25$. The strain tensor components b) ϵ^{γ}_{xy} c) ϵ^{γ}_{xx}, d) ϵ^{γ}_{yy}.

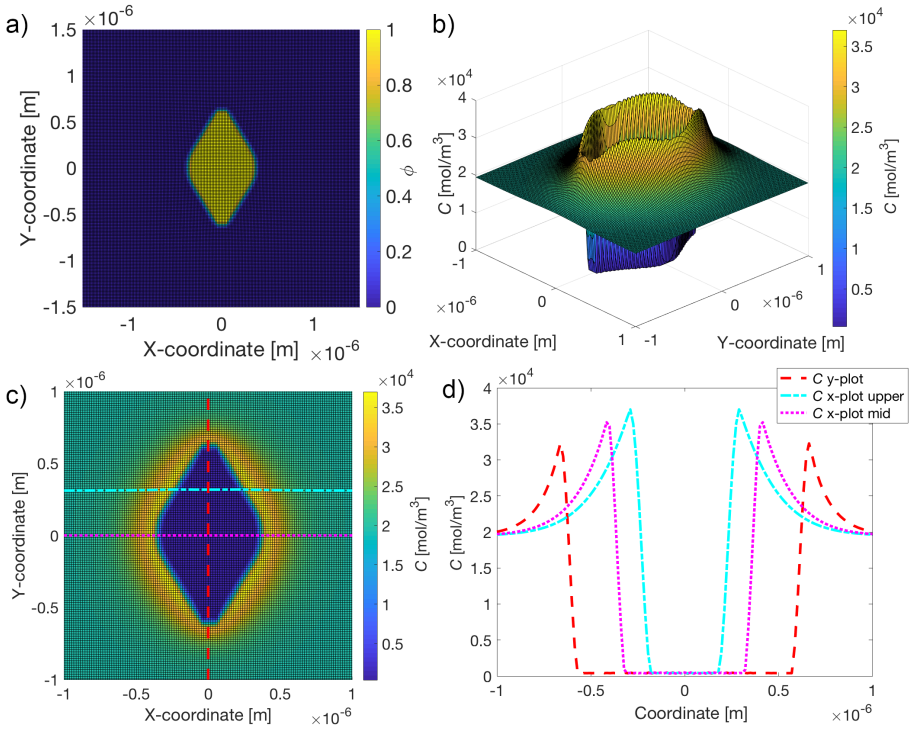

Figure 13: The carbon concentration near the ferrite region a), which nucleated and grew at grain face. b) 3-D plot of the concentration, c) the concentration was analyzed along three different lines, the plots are shown in d).

It can be seen that those interfaces, which were oriented along the grain boundary line, propagated fastest, and they contain the least carbon. This shows that the carbon is transported to the sides of the rapidly propagating interface. Since lower carbon concentration at the interface yields faster interface propagation, this effect introduces self-reinforcing feedback loop. Those fronts that initially propagate faster contain less carbon than the slowly propagating fronts and as a result, their propagation speed becomes faster than the initially slowly propagating boundaries.

A similar simulation of a ferrite region nucleated at a grain edge (i.e. the interface of three austenite grains) was conducted. Since grain edges can have even higher energy state, due to the lattice mismatch of the austenite grains, they are even more probable nucleation sites than flat grain faces. However, grain faces are more abundant than the grain edges. The simulation snapshots for this case are shown in Fig. 14, where the location of the initial austenite grain boundaries are again depicted with the red dashed line.

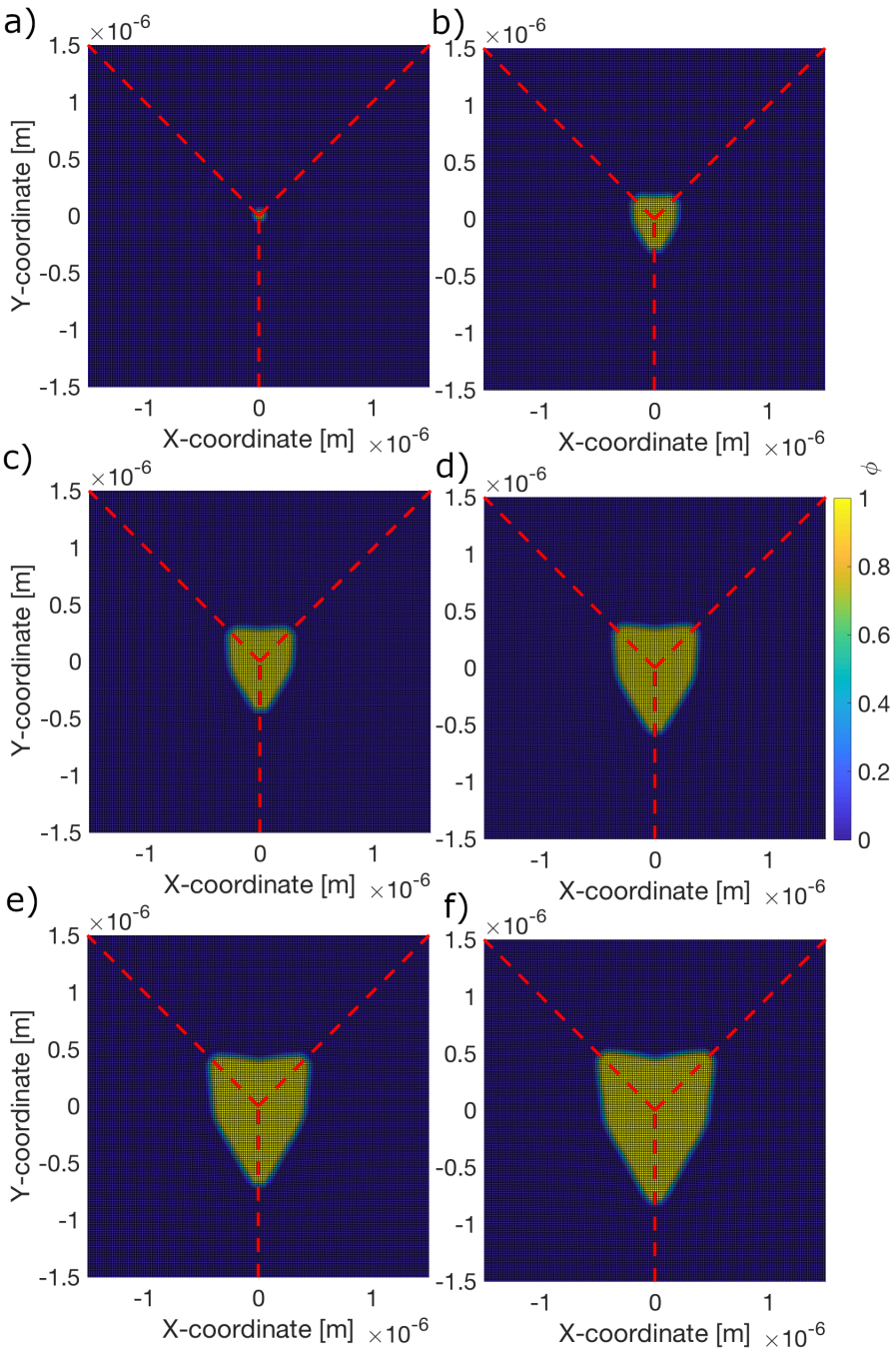

Figure 14: Growth of a ferrite region nucleated at a grain edge. The grain boundaries are depicted with a red dashed line. Simulation snapshots at time instants a) $t = 0.0047$ s, b) $t = 0.0518$ s, c) $t = 0.0859$ s, d) $t = 0.1187$ s, e) $t = 0.1358$ s, f) $t = 0.1837$ s.

5.6 Numerical experiment 6: Growth of homogeneously nucleated bainite subunit

Until now, all the described simulations have considered austenite to ferrite transformation due to diffusional mechanism, which leads to isotropic expansion. However, the austenite transformation to bainitic ferrite occurs through shear mechanism, and leads to a different strain state, the invariant plane strain. The associated non-zero eigenstrains for the bainite formation are $\sigma^{00}_{yy} = 0.03$, $\sigma^{00}_{xy} = 0.26$. [43, 44] The parameter $\lambda = 0.5$ was used for the results described here. Increasing the value of lambda to 1 yielded thinner structure, but otherwise similar elongated shape resulted. Temperature was set to $T = 500$ °C, which is realistic for formation of upper bainite. In the same way as earlier, an interesting insight to the transformation mechanism can be obtained by considering a simple case, where the bainite is assumed to be homogeneously nucleated in the surrounding austenite. These results can then be compared to a more realistic case, where the bainite is nucleated at the grain boundary, section 5.7.

The simulation for the growth of a bainite subunit which had been homogeneously nucleated at the austenite was conducted. The simulation snapshots at different times are shown in Fig. 15. The bainite subunit grows much faster in the x-direction, as the growth in the y-direction is almost fully diminished. Although the current simulations are made in two dimensional plane strain conditions, the result is in agreement with the fact that the bainite subunits form as platelets in reality [45].

The reason for the formation of the subunit shape can be understood by mechanical energy that is required for the transformation to proceed and the austenite strains, which are illustrated in Fig. 16. The bainite eigenstrains cause the neighbouring austenite in the x-direction to bend towards the eigenstrain state. As a result, the mechanical energy barrier, calculated using Eq. (20), is diminished, and the interface propagates rapidly in the x-direction. In contrast, the bainite eigenstrains cause the neighbouring austenite in y-direction to bend against the eigenstrain state. For this reason the energy barrier is increased, and the growth in y-direction is diminished.

The carbon concentration in the neigbourhood of the bainite subunit is analyzed in Fig. 17 for the time instant $t = 0.0214$ s, shown in a). The 3D-plot of the concentration field b) shows the overall shape of the field near the bainite-austenite interface. The concentration was plotted along the lines shown in c). The plots are shown in d). Although the nonuniform growth of the bainite subunit occurs initially due to the eigenstrains which are created through the shear transformation mechanism, it can be seen that the carbon concentration is lowest at the interface directions where the growth rate was fastest, similar to what was observed for the formation of ferrite at the grain boundary (section 5.5). Similarly here, the carbon seems to be transported to the sides of the rapidly progressing interface. Since lower carbon concentration yields higher propagation speed, this mechanism can result to self reinforcing feedback loop.

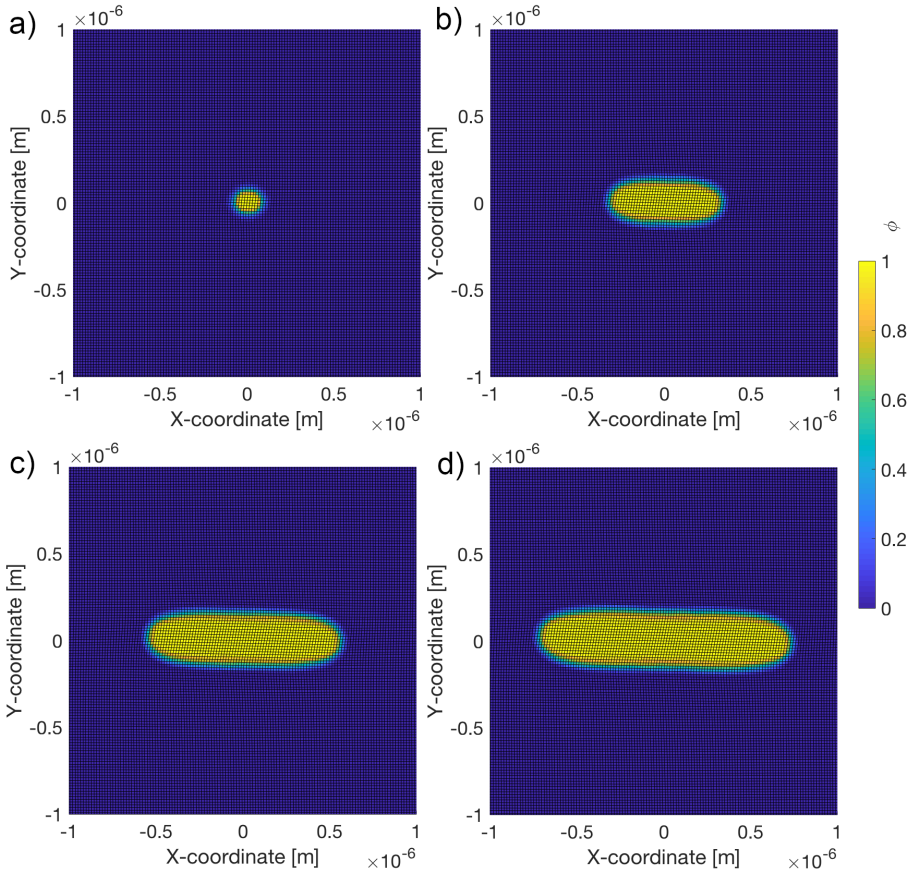

Figure 15: Growth of a bainite subunit which was assumed to have been homogeneously nucleated in surrounding austenite. The simulation snapshots at time instants a) 0.0042 s, b) 0.0214 s, c) 0.0343 s d) 0.0430 s.

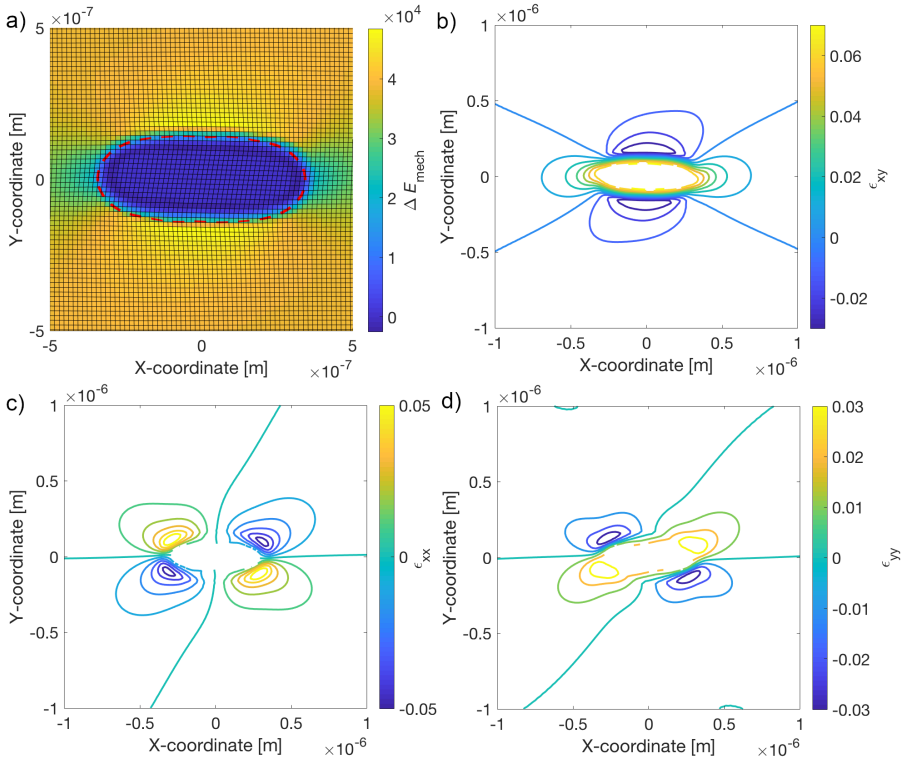

Figure 16: a) Change of mechanical energy due to transformation calculated with Eq. (20) for a homogeneosly nucleated bainite depicted in Fig. 15 b). The red dashed line shows contour for $\phi = 0.25$. The strain tensor components b) ϵ^{γ}_{xy} c) ϵ^{γ}_{xx}, d) ϵ^{γ}_{yy}. The non-zero bainite eigenstrains were $\epsilon^{00}_{yy} = 0.03$, $\epsilon^{00}_{xy} = 0.26$.

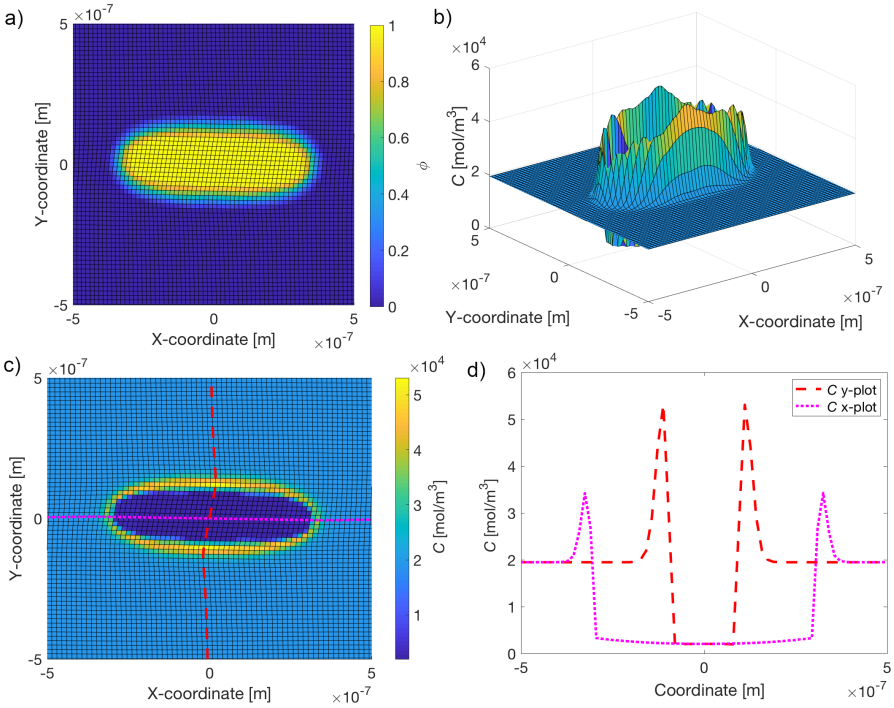

Figure 17: The carbon concentration was analyzed near a bainite subunit a), which had homogeneously nucleated and grew to the surrounding austenite. b) 3-D plot of the concentration field, c) the concentration was analyzed along two different lines, the plots are shown in d).

5.7 Numerical experiment 7: Growth of bainite nucleated at a grain boundary

Similarly to the ferrite case, the bainite nucleation usually occurs at crystal defects, such as grain boundaries. The grain boundary was defined in the simulation domain as indicated with the vertical red dashed line in Fig. 18. The bainite nucleus was initiated in the middle of the grain boundary in the y-direction. Similarly to the earlier case (section 5.5), it is assumed that the removal of the austenite grain boundary due to bainite growth yields a change of -15 kJ/mol in the energy barrier for interface propagation for the gridpoints that are contained in the grain boundary. The simulation snapshots at different times are shown in the Fig. 18. The initial bainite subunite grew along the x-direction in a similar way as previous case (section 5.6). At the same time, the bainitic region grew along the vertical grain boundary, b) and c). Once the vertical growth had proceeded sufficiently far away from the initial subunit, another subunit started to form below the first one, d). Both of the subunits grew along the x-direction. Finally, a third subunit started to form below the

second subunit, f). This mechanism appears to lead to formation of parallel subunits at the prior austenite grain boundary. The bainite growth reached the boundaries of the simulation domain that were held fixed. In future studies, the simulation parameters could be calibrated using experimental data for bainite growth speed and the resulting morphology, to obtain realistic values for the model.

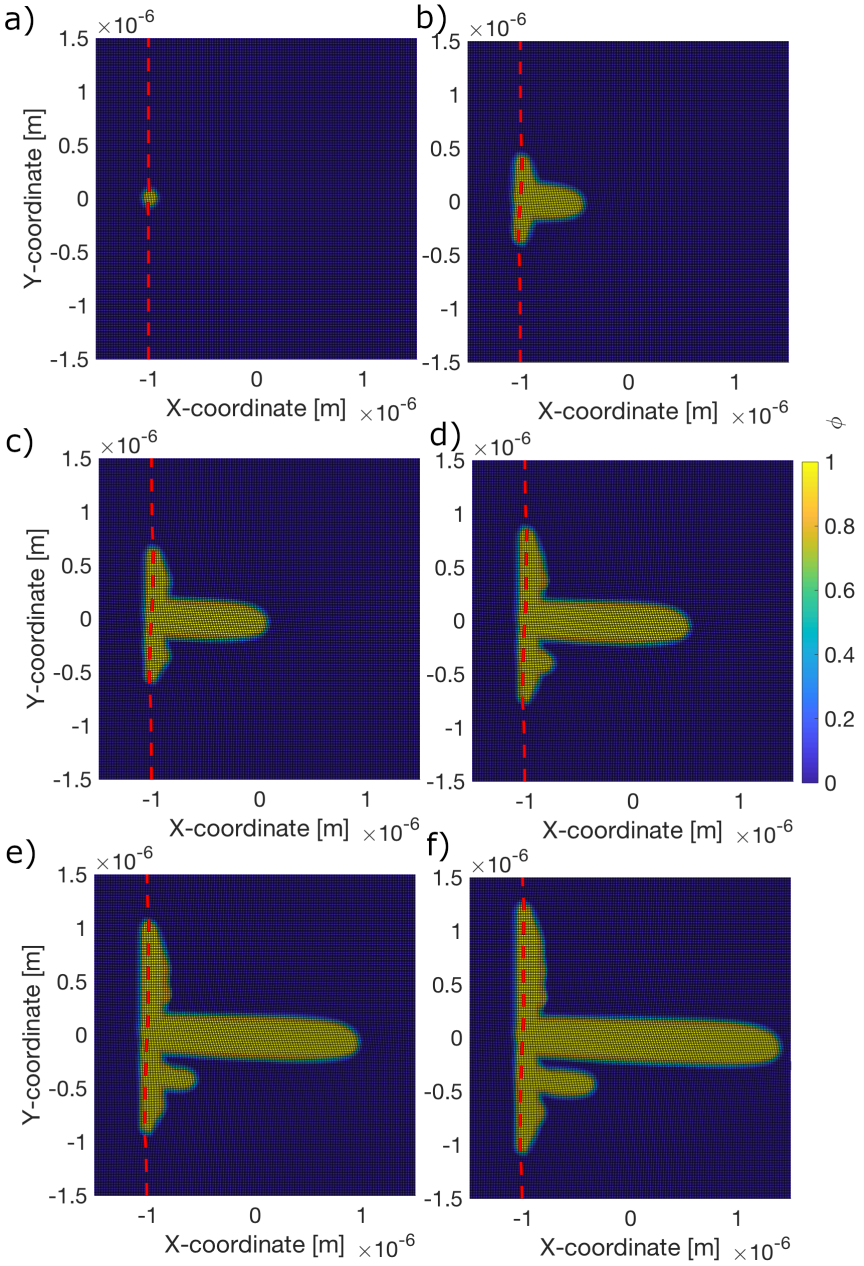

Figure 18: Growth of a bainite region nucleated at a grain boundary. The grain boundary is depicted with a red dashed line. Simulation snapshots at time instants a) $t = 0.0025$ s, b) $t = 0.0402$ s, c) $t = 0.0663$ s, d) $t = 0.0888$ s, e) $t = 0.1101$ s, f) $t = 0.1318$ s.

The close up of the carbon concentration field for the final simulation snapshot (18 f)) around the second initiated sub-unit is shown in 19 a). The concentration was plotted along the horizontal magenta and the vertical cyan line and the plots are shown in b). The field describing the mechanical energy required for the phase transformation to complete is shown in Fig. 19 c) and the field values are plotted along the indicated lines in d). It can be seen from b) and d) that the austenite region, which is located between the bainite subunits (y-coordinate between -0.37 μm and -0.15 μm) is enriched with carbon and the mechanical energy for the transformation is higher than at the tip of the bainite sub-unit. This calculation result indicates that the austenite between the subunits becomes chemically and mechanically stabilized [3]. Although the model was not accurately parameterized by experimental or thermodynamic data in the current study, this result demonstrates that the model qualitatively reproduces realistic phenomena.

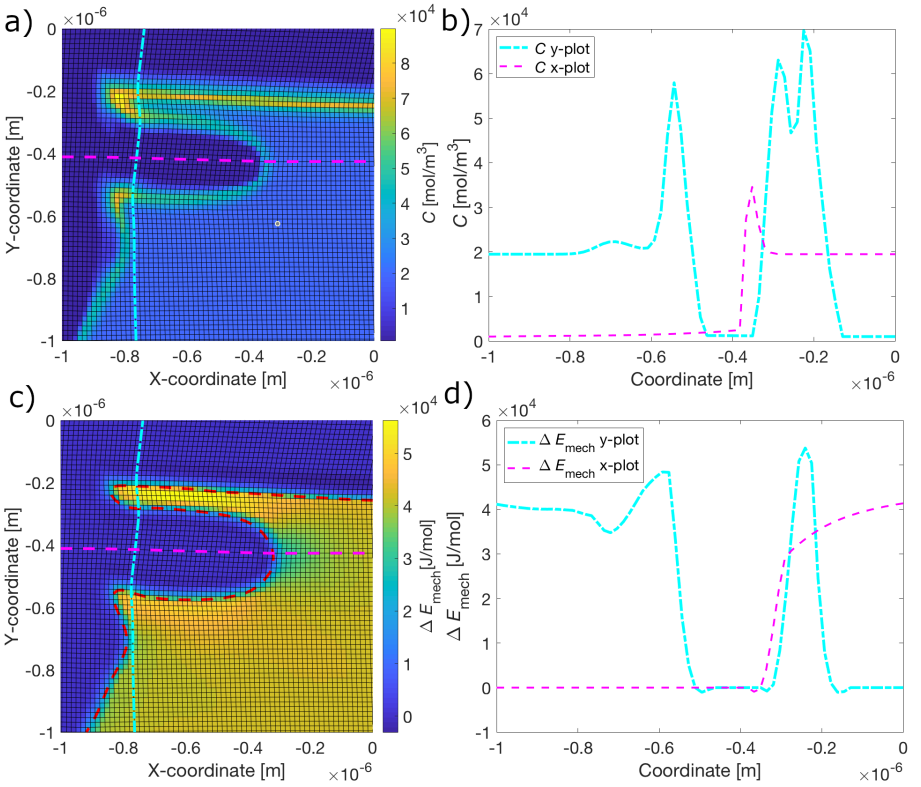

Figure 19: The region [-1 μm, 0]×[[-1 μm, 0]] of the simulation snapshot shown in Fig. 18 f). a) The carbon concentration field, where the concentration was plotted along the horizontal dashed magenta line and the vertical cyan line. The plots are shown in b). c) The mechanical energy change required for the phase transformation to complete, ΔE_{mech}, the plots along the lines are shown in d).The contour of $\phi = 0.25$ is shown with red dashed line in c).

6 Summary, conclusions and outlook

A mathematical model for calculation of the elastic strains, partitioning and diffusion and propagation of a phase front was described. The solutions of the equations describing the phenomena provide a coupled model. The coupled model allows to simulate the dynamical evolution of the system. The speed of the phase front propagation was derived from the concept of thermal activation and it was used in the numerical examples instead of the widely used Allen-Cahn equation. However, the connection to the Allen-Cahn equation was made, which would allow for its use also in a similar way. A new equation for describing the effect of strains on the activation energy barrier was derived, which includes description for the different elastic constants for austenite and ferrite.

The numerical procedure for solving the equations and the calculation of the phase propagation was described. Numerical experiments for selected cases were conducted: the elastostatic solution was compared to an analytic solution for the stresses surrounding an expanded elastic cylinder; the partitioning and diffusion of carbon from ferrite to austenite was compared to the previously applied sharp interface model; isotropic growth of homogeneously nucleated ferrite was calculated. The aim of these examples was to compare the implemented model to the known solutions. The applicability of the model in a few interesting conditions was furher tested: the growth of allotriomorphic ferrite, nucleated on grain boundary and grain edge were calculated; the growth of a bainite sub-unit, and the growth of bainitic region that was initiated on a grain boundary were simulated. In the current study, the aim was to describe the mathematical model and the numerical solution procedure. The model parameters were chosen to show the operation of the mathematical model, but they were not calibrated against experimental data in the current study. This is the aim of future research.

The developed model allows the inclusion of the relevant physical phenomena to the morphological evolution of phase growth in solid to solid phase transformations. The length and time scales that are attainable by the model are between the atomistic and macroscopic scales. In future the model could be partially be parameterized using atomistic simulations and partially using experimental data. This approach would allow for the development of fundamentally physical science based model, which would include the relevant phenomena from the atomistic length scales and predict the experimentally observed morphological evolution of the phase formation. Also in the future, other important phenomena could be introduced to the model, such as segregation of carbon to dislocations and the formation of carbides [40] and the plastic relaxation of the elastic strains in the austenite [6] as well as nucleation of new subunits in the austenite in the vicinity of the growing sub-unit tip [46].

7 Acknowledgments

The funding of this research activity under the auspices of Genome of Steel (Profi3) project through grant #311934 by the Academy of Finland is gratefully acknowledged.

References

[1] Joonas Ilmola, Aarne Pohjonen, Sami Koskenniska, Oskari Seppälä, Olli Leinonen, Juha Jokisaari, Juha Pyykkönen, and Jari Larkiola. Coupled heat transfer and phase transformations of dual-phase steel in coil cooling. *Materials Today Communications*, 26:101973, 2021.

[2] Vahid Javaheri, Aarne Pohjonen, John Inge Asperheim, Dmitry Ivanov, and David Porter. Physically based modeling, characterization and design

of an induction hardening process for a new slurry pipeline steel. *Materials & Design*, 182:108047, 2019.

[3] Aarne Pohjonen, Pentti Kaikkonen, Oskari Seppälä, Joonas Ilmola, Vahid Javaheri, Timo Manninen, and Mahesh Somani. Numerical and experimental study on thermo-mechanical processing of medium-carbon steels at low temperatures for achieving ultrafine-structured bainite. *Materialia*, 18:101150, 2021.

[4] Mathieu Bouville and Rajeev Ahluwalia. Interplay between diffusive and displacive phase transformations: Time-temperature-transformation diagrams and microstructures. *Physical review letters*, 97(5):055701, 2006.

[5] Irina Loginova. *Phase-field modeling of diffusion controlled phase transformations*. PhD thesis, Mekanik, 2003.

[6] Amer Malik. *Phase change with stress effects and flow*. PhD thesis, KTH Royal Institute of Technology, 2013.

[7] Amer Malik, Gustav Amberg, Annika Borgenstam, and John Ågren. Effect of external loading on the martensitic transformation–a phase field study. *Acta materialia*, 61(20):7868–7880, 2013.

[8] Krzysztof Bzowski, Lukasz Rauch, and Maciej Pietrzyk. Application of statistical representation of the microstructure to modeling of phase transformations in dp steels by solution of the diffusion equation. *Procedia Manufacturing*, 15:1847–1855, 2018.

[9] Danuta Szeliga, Krzysztof Bzowski, Łukasz Rauch, Roman Kuziak, and Maciej Pietrzyk. Mean field and full field modelling of microstructure evolution and phase transformations during hot forming and cooling of low carbon steels. *Computer Methods in Materials Science*, 20(3):122, 2020.

[10] E Javierre Perez. *Numerical methods for vector Stefan models of solid-state alloys*. Delft University of Technology, 2006.

[11] M.M. Moghadam and P.W. Voorhees. Level-set simulation of anisotropic phase transformations via faceted growth. *Computational Materials Science*, 143:454–461, 2018.

[12] Dong An, Shiyan Pan, Li Huang, Ting Dai, Bruce Krakauer, and Mingfang Zhu. Modeling of ferrite-austenite phase transformation using a cellular automaton model. *ISIJ international*, 54(2):422–429, 2014.

[13] Jarosław Opara and Roman Kuziak. Study of phase transformations in complex phase steel using a mesoscale cellular automaton model part 1: Modeling fundamentals. *Journal of Metallic Materials*, 72(3), 2020.

[14] Oskari Seppälä, Aarne Pohjonen, Antti Kaijalainen, Jari Larkiola, and David Porter. Simulation of bainite and martensite formation using a novel cellular automata method. *Procedia Manufacturing*, 15:1856–1863, 2018.

[15] Oskari Seppälä, Aarne Pohjonen, and Jari Larkiola. Effect of anisotropic growth and grain boundary impingement on bainite transformation models. *Proceedings of The 61st SIMS Conference on Simulation and Modelling SIMS 2020, September 22-24, Virtual Conference, Finland*, 2021.

[16] JW Cahn and SM Allen. A microscopic theory for domain wall motion and its experimental verification in fe-al alloy domain growth kinetics. *Le Journal de Physique Colloques*, 38(C7):C7–51, 1977.

[17] John W Cahn. On spinodal decomposition. *Acta metallurgica*, 9(9):795–801, 1961.

[18] John W Cahn and John E Hilliard. Free energy of a nonuniform system. i. interfacial free energy. *The Journal of chemical physics*, 28(2):258–267, 1958.

[19] Junseok Kim, Seunggyu Lee, Yongho Choi, Seok-Min Lee, and Darae Jeong. Basic principles and practical applications of the cahn–hilliard equation. *Mathematical Problems in Engineering*, 2016, 2016.

[20] Yuhong Zhao, Bing Zhang, Hua Hou, Weipeng Chen, and Meng Wang. Phase-field simulation for the evolution of solid/liquid interface front in directional solidification process. *Journal of Materials Science & Technology*, 35(6):1044–1052, 2019.

[21] Felix Diewald, Michaela Heier, Martin Horsch, Charlotte Kuhn, Kai Langenbach, Hans Hasse, and Ralf Müller. Three-dimensional phase field modeling of inhomogeneous gas-liquid systems using the pets equation of state. *The Journal of Chemical Physics*, 149(6):064701, 2018.

[22] Valeria Berti, Mauro Fabrizio, and Diego Grandi. A phase field model for liquid-vapour phase transitions. *Discrete and Continuous Dynamical Systems - S*, 6(2):317–330, 2013.

[23] Hans-Dieter Alber and Peicheng Zhu. Comparison of a rapidely converging phase field model for interfaces in solids with the allen-cahn model. *Journal of Elasticity*, 111(2):153–221, 2013.

[24] Nele Moelans, Bart Blanpain, and Patrick Wollants. An introduction to phase-field modeling of microstructure evolution. *Calphad*, 32(2):268–294, 2008.

[25] Jaber Rezaei Mianroodi, Pratheek Shanthraj, Chuanlai Liu, Samad Vakili, Sharan Roongta, Nima Hamidi Siboni, Nathan Perchikov, Yang Bai, Bob Svendsen, Franz Roters, et al. Modeling and simulation of microstructure in metallic systems based on multi-physics approaches. *npj Computational Materials*, 8(1):1–15, 2022.

[26] Georges-Henri Cottet and Emmanuel Maitre. A level set method for fluid-structure interactions with immersed surfaces. *Mathematical models and methods in applied sciences*, 16(03):415–438, 2006.

[27] Danai Polychronopoulou, Nathalie Bozzolo, D Pino Muñoz, Julien Bruchon, Modesar Shakoor, Yvon Millet, Christian Dumont, I Freiherr von Thüngen, Rémy Besnard, and Marc Bernacki. Introduction to the level-set full field modeling of laths spheroidization phenomenon in α/β titanium alloys. *International Journal of Material Forming*, 12(2):173–183, 2019.

[28] J.W. CHRISTIAN. Chapter 11 - theory of thermally activated growth. In J.W. Christian, editor, *The Theory of Transformations in Metals and Alloys*, pages 480–528. Pergamon, Oxford, 2002.

[29] Phong Dao, Bilal Latif, and Lu Zhao **Online document**. Theories of reaction rates, libretext. `https://chem.libretexts.org/Bookshelves/Physical_and_Theoretical_Chemistry_Textbook_Maps/Map\%3A_Physical_Chemistry_for_the_Biosciences_(Chang)/09\%3A_Chemical_Kinetics/9.07\%3A_Theories_of_Reaction_Rates`. Accessed: 2021-7-7.

[30] MG Mecozzi, J Sietsma, S Van Der Zwaag, M Apel, P Schaffnit, and I Steinbach. Analysis of the $\gamma \rightarrow \alpha$ transformation in a c-mn steel by phase-field modeling. *Metallurgical and Materials Transactions A*, 36(9):2327–2340, 2005.

[31] Lev Davidovich Landau, Evgenij M Lifšic, Evegnii Mikhailovich Lifshitz, Arnold Markovich Kosevich, and Lev Petrovich Pitaevskii. *Theory of elasticity: volume 7*, volume 7. Elsevier, 1986.

[32] Yilin Wang, Huicheng Geng, Bin Zhu, Zijian Wang, and Yisheng Zhang. Carbon redistribution and microstructural evolution study during two-stage quenching and partitioning process of high-strength steels by modeling. *Materials*, 11(11), 2018.

[33] Arman Ghasemi, Penghao Xiao, and Wei Gao. Nudged elastic band method for solid-solid transition under finite deformation. *The Journal of Chemical Physics*, 151(5):054110, 2019.

[34] Aarne Pohjonen. Solving partial differential equations in deformed grids by estimating local average gradients with planes. *Journal of Physics: Conference Series*, 2090(1):012069, nov 2021.

[35] Neil Gershenfeld. *The Nature of Mathematical Modeling*. Cambridge University Press, 2011.

[36] Aarne Pohjonen. Numerical experiments on the solution of advection equation for moving phase interface: encountered problems and their solutions, accepted for publication in ic-msquare 2022 conference proceedings. *AIP Conference Proceedings*, 2022.

[37] **Online document**. Matlab documentation. `https://se.mathworks.com/help/matlab/`. Accessed: 2021-5-10.

[38] P Kelly. Solid mechanics part ii: Engineering solid mechanics. *https://pkel015.connect.amazon.auckland.ac.nz/SolidMechanicsBooks/Part_II/index.html*, 2018.

[39] X-W Yu, Z-W Wang, H Wang, and N-Y Leng. Eshelby's circular cylindrical inclusion with polynomial eigenstrains in transverse direction by residue theorem. *Archive of Applied Mechanics*, 91(4):1437–1447, 2021.

[40] Aarne Pohjonen, Shashank Ramesh Babu, and Ville-Valtteri Visuri. Coupled model for carbon partitioning, diffusion, cottrell atmosphere formation and cementite precipitation in martensite during quenching. *Computational Materials Science*, 209:111413, 2022.

[41] Harshad KDH Bhadeshia. Diffusional formation of ferrite in iron and its alloys. *Progress in Materials Science*, 29(4):321–386, 1985.

[42] David Porter. *Phase Transformations in Metals and Alloys, 4th Edition*. CRC Press, 2022.

[43] MJ Peet and HKDH Bhadeshia. Surface relief due to bainite transformation at 473 k (200° c). *Metallurgical and Materials Transactions A*, 42(11):3344–3348, 2011.

[44] E Swallow and HKDH Bhadeshia. High resolution observations of displacements caused by bainitic transformation. *Materials Science and Technology*, 12(2):121–125, 1996.

[45] H.K.D.H Bhadeshia. Chapter 2 - bainitic ferrite. In *Bainite In Steels, 2nd Edition*, pages 19–60. The Unversity Press, Cambridge, 2001.

[46] T.T. Arif and R.S. Qin. A phase-field model for bainitic transformation. *Computational Materials Science*, 77:230–235, 2013.